iScience

CellPress
OPEN ACCESS

Article

Two-Dimensional Titanium and Molybdenum Carbide MXenes as Electrocatalysts for CO_2 Reduction

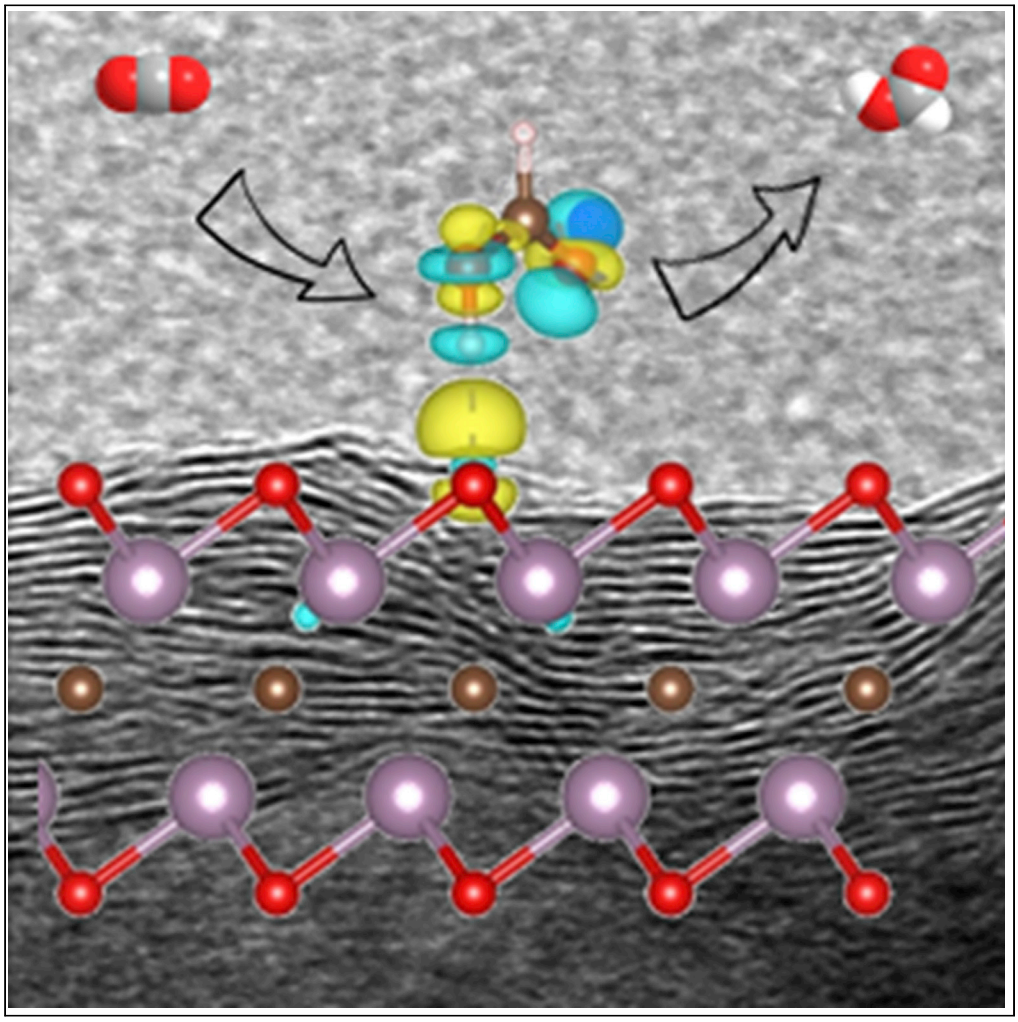

Albertus D. Handoko, Hetian Chen, Yanwei Lum, Qianfan Zhang, Babak Anasori, Zhi Wei Seh

qianfan@buaa.edu.cn (Q.Z.)
banasori@iupui.edu (B.A.)
sehzw@imre.a-star.edu.sg (Z.W.S.)

HIGHLIGHTS

Combined experimental and theoretical CO_2RR investigation on MXenes

T_x group stabilizes *H-coordinated intermediates and breaks scaling relations

Formic acid is the main CO_2RR product on Ti_2CT_x and Mo_2CT_x MXenes

Lower degree of –F termination in T_x group results in smaller overpotential

Handoko et al., iScience *23*, 101181
June 26, 2020
https://doi.org/10.1016/j.isci.2020.101181

iScience

CellPress
OPEN ACCESS

Article

Two-Dimensional Titanium and Molybdenum Carbide MXenes as Electrocatalysts for CO_2 Reduction

Albertus D. Handoko,[1] Hetian Chen,[2] Yanwei Lum,[1] Qianfan Zhang,[2,*] Babak Anasori,[3,4,*] and Zhi Wei Seh[1,5,*]

SUMMARY

Electrocatalytic CO_2 reduction reaction (CO_2RR) is an attractive way to produce renewable fuel and chemical feedstock, especially when coupled with efficient CO_2 capture and clean energy sources. On the fundamental side, research on improving CO_2RR activity still revolves around late transition metal-based catalysts, which are limited by unfavorable scaling relations despite intense investigation. Here, we report a combined experimental and theoretical investigation into electrocatalytic CO_2RR on Ti- and Mo-based MXene catalysts. Formic acid is found as the main product on Ti_2CT_x and Mo_2CT_x MXenes, with peak Faradaic efficiency of over 56% on Ti_2CT_x and partial current density of up to -2.5 mA cm^{-2} on Mo_2CT_x. Furthermore, simulations reveal the critical role of the T_x group: a smaller overpotential is found to occur at lower amounts of –F termination. This work represents an important step toward experimental demonstration of MXenes for more complex electrocatalytic reactions in the future.

INTRODUCTION

Efforts to tackle rising CO_2 concentration in the atmosphere have been primarily focused on carbon capture and sequestration, as well as decarbonization of the energy and land use sectors (Walsh et al., 2017). However, an equally pressing issue of depleting fossil energy and chemical raw materials is looming. Electrocatalytic CO_2 reduction reaction (CO_2RR) presents an attractive pathway to achieve both decarbonization of energy economy and production of renewable fuel/chemical feedstock (De Luna et al., 2019; Seh et al., 2017), especially when coupled with increasingly affordable clean electricity (Obama, 2017).

To realize industrial-scale CO_2RR, substantial challenges on both the fundamental (i.e., catalyst activity and selectivity) and system levels (i.e., mass transport, conversion rate, and energy efficiency) need to be addressed (Jouny et al., 2018; De Luna et al., 2019; Handoko et al., 2018c; Higgins et al., 2019). On the fundamental side, there has been some progress in understanding CO_2RR in liquid electrolytes, with emphasis on late transition metals, particularly copper, owing to its unusual ability to convert CO_2 to multi-carbon products (Hori, 2008; Huang et al., 2017). However, despite intense optimization of these transition metal catalysts (Saberi Safaei et al., 2016; Handoko et al., 2016; Mistry et al., 2016; Li et al., 2017b; Ren et al., 2016), their activity and selectivity seem to be limited. One of the most significant barriers limiting fundamental CO_2RR on transition metal catalysts appears to be the linear scaling relations between the binding energies of reaction intermediates (Liu et al., 2017). These unfavorable scaling relations due to similarly bound reaction intermediates (e.g., *COOH, *CO, *CHO, "*" refers to a site on the catalyst surface) limit the CO_2RR overpotential that can be achieved on pure transition metal surfaces.

One of the most promising ways to improve CO_2RR activity is to explore new catalyst material systems that allow stabilization of intermediates with different scaling relations. MXenes, a family of two-dimensional transition metal carbide/nitride materials with metallic-like conductivity (Anasori et al., 2017), present a viable solution. MXenes have a general formula of $M_{n+1}X_nT_x$, where M represents an early transition metal, X is carbon and/or nitrogen, with n in the range of 1–4 (Anasori and Gogotsi, 2019; Deysher et al., 2020). T_x represents surface termination groups, which can include –O, –F, etc. (Hope et al., 2016). The tunable surface and internal configuration of MXenes, including the possibility of mixed surface terminations, as well as mixed metal atoms in solid solution (Yang et al., 2016) or ordered structure (Anasori et al., 2015; Anasori and Gogotsi, 2019), allow for tailoring of intermediates' binding configuration and strength (Hart et al., 2019; Anasori et al., 2016; Handoko et al., 2018a; Chen et al., 2019), making it an ideal platform to search for active and selective CO_2RR catalysts (Handoko et al., 2019). To date, investigations of MXenes for

[1]Institute of Materials Research and Engineering, Agency for Science, Technology and Research (A*STAR), 2 Fusionopolis Way, Innovis, Singapore 138634, Singapore

[2]School of Materials Science and Engineering, Beihang University, Beijing, 100191, P. R. China

[3]Department of Mechanical and Energy Engineering, Integrated Nanosystems Development Institute, Indiana University–Purdue University Indianapolis, Indianapolis, IN 46202, USA

[4]A.J. Drexel Nanomaterials Institute and Department of Materials Science and Engineering, Drexel University, Philadelphia, PA 19104, USA

[5]Lead Contact

*Correspondence: qianfan@buaa.edu.cn (Q.Z.), banasori@iupui.edu (B.A.), sehzw@imre.a-star.edu.sg (Z.W.S.)

https://doi.org/10.1016/j.isci.2020.101181

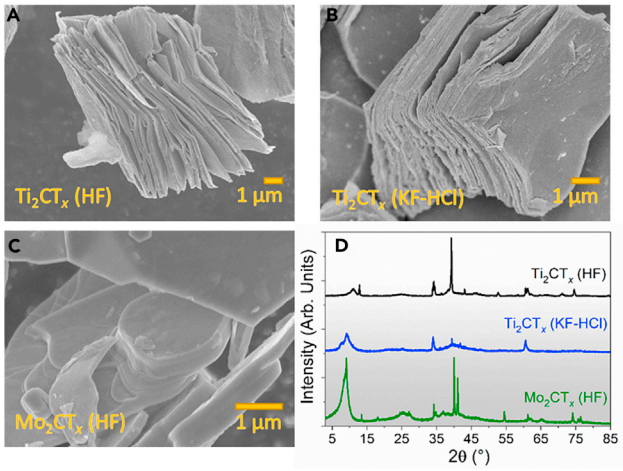

Figure 1. Morphology and Phase Characterization of Ti_2CT_x and Mo_2CT_x MXenes

Scanning electron micrographs of as-synthesized (A) Ti_2CT_x (HF), (B) Ti_2CT_x (KF-HCl), and (C) Mo_2CT_x (HF) and (D) the corresponding X-ray diffraction data.

electrocatalytic CO_2RR have been primarily based on theoretical calculations (Li et al., 2017a; Handoko et al., 2018b; Chen et al., 2019; Zhang et al., 2017b), although some works on photocatalytic CO_2RR have indicated that MXenes may enhance charge separation or act as co-catalyst (Cao et al., 2018; Ye et al., 2018).

Here, we investigate the electrocatalytic CO_2RR activity on Ti_2CT_x and Mo_2CT_x MXenes using a combination of experiment and theory. These MXenes were chosen as they have Ti and Mo metal sites with opposing hydrogen binding behavior (Laursen et al., 2012). The CO_2RR experiments are carried out in mixtures of acetonitrile, water, and 3-butyl-1-methyl-1H-imidazol-3-ium tetra-fluoroborate ($BMIMBF_4$) electrolyte. Formic acid is found to be the main CO_2RR product on these MXenes with Faradaic efficiency of 56.1% at −1.8 V (all potentials in this work are expressed with respect to the standard hydrogen electrode, SHE). H_2 is the main side product, alongside trace amounts of CO, CH_4, and other hydrocarbons. More importantly, we demonstrate that the nature of surface terminating group appears to control the CO_2RR activity. Specifically, the presence of –F termination group, commonly adsorbed onto MXene surface during synthesis (Hope et al., 2016), was found to alter the binding strength of intermediates and the corresponding CO_2RR limiting potential compared to fully –O terminated MXenes, as supported by density functional theory (DFT). Overall, this work provides insights on MXene electrocatalysts that circumvent traditional scaling relations in CO_2RR, which can potentially be extended to other promising reactions of interest.

RESULTS

We first investigate the effect of surface termination group T_x on the CO_2RR activity of Ti_2CT_x MXenes. To achieve this, we synthesized two variants of Ti_2CT_x with different surface termination compositions using different etching procedures, namely, 18 h in 10% HF and 48 h in 4 M KF-HCl mixture (refer to the Transparent Methods in the Supplemental Information). These MXenes will be referred to as Ti_2CT_x (HF) and Ti_2CT_x (KF-HCl), respectively. Previous works suggest that the use of fluoride salt etching solution in place of HF can reduce the amounts of –F terminations (Hope et al., 2016; Handoko et al., 2018a). The scanning electron micrographs of both Ti_2CT_x (HF) and Ti_2CT_x (KF-HCl) show layered structures after the etching procedure (Figures 1A and 1B), consistent with previously reported morphologies (Anasori et al., 2017). X-ray diffraction (XRD) shows that most of the Ti_2AlC precursors are successfully converted to Ti_2CT_x, with the appearance of the characteristic (002) broad peaks of MXenes around $2\theta = 11.1°$ and 9.2° for HF and KF-HCl etched Ti_2CT_x, respectively (Figure 1D; see Figure S1 and Table S1 for characterization of precursors). These peaks correspond to MXene interlayer distances of around 8.0 and 9.6 Å, consistent with previous reports on smaller interlayer distance for HF-etched samples Naguib et al., 2012.

X-ray photoelectron spectroscopy (XPS) of the as-synthesized Ti_2CT_x samples in the Ti *2p* range detects a mix of Ti species, including Ti-T_x/C, Ti(II), and more oxidized Ti(IV) species (Figures 2A and 2B; see Tables

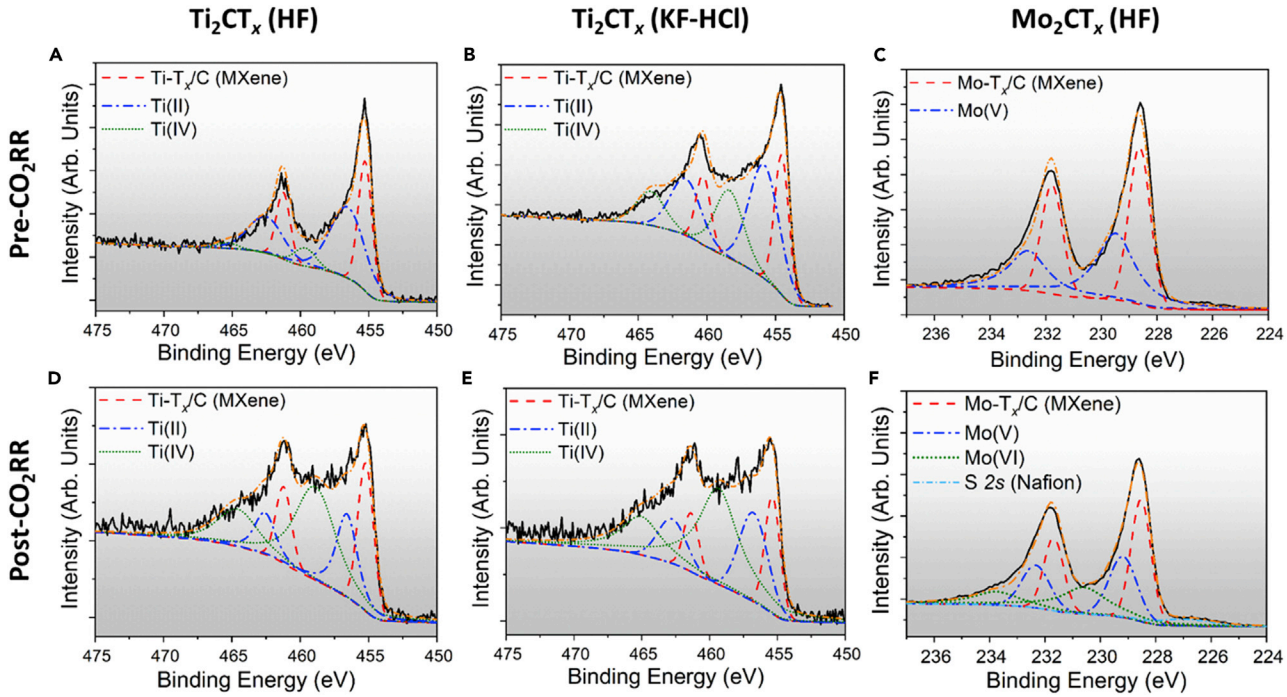

Figure 2. Analysis of the "M" Elements of Ti_2CT_x and Mo_2CT_x MXenes

X-ray photoelectron spectroscopy measurements of MXenes before and after CO_2RR: (A and D) Ti *2p* spectra of Ti_2CT_x (HF), (B and E) Ti *2p* spectra of Ti_2CT_x (KF-HCl), (C and F) Mo *3d* spectra of Mo_2CT_x (HF).

S2–S5 for more details). Some degree of Ti(IV) formation is unavoidable in Ti_2CT_x as it is less stable against oxidation compared with other MXenes with higher *n* such as $Ti_3C_2T_x$ (Zhang et al., 2017a). A comparison of the F to Ti atomic ratio (Tables S3 and S4) shows that Ti_2CT_x (HF) has significantly more –F surface terminations (F/Ti = 0.36) than Ti_2CT_x (KF-HCl) (F/Ti = 0.21). We have previously shown that the electrocatalytic activities of MXenes are very sensitive to the surface termination (Handoko et al., 2018a), thus we posit that the variation in –F termination content on Ti_2CT_x samples will alter their CO_2RR activity.

As an initial CO_2RR activity assessment, we first compared the linear scanning voltammetry (LSV) profile of Ti_2CT_x (HF) and Ti_2CT_x (KF-HCl) in the presence and absence of CO_2 in a mixture of 80:15:5 mol fraction of acetonitrile:water:$BMIMBF_4$ electrolyte (Figure S2). The electrolyte mixture is used in this study owing to prevalent HER in aqueous electrolyte systems like 0.1 M $KHCO_3$ (Figure S3). Dipolar aprotic solvents like acetonitrile have enhanced CO_2 solubility compared with aqueous systems (Gennaro et al., 1990). Furthermore, imidazolium-based ionic liquid has been shown to enhance CO_2RR (Asadi et al., 2016), possibly by forming complexes with CO_2 molecules at moderately cathodic potentials (−0.1 V versus SHE) (Matsubara et al., 2015; Rosen et al., 2011).

Under N_2 purging, both Ti_2CT_x samples display sharp onset potential at around −1.8 V (Figures S2A and S2B), which can be attributed to the hydrogen evolution reaction (HER). The introduction of CO_2 into the reaction environment changes the LSV profile for both Ti_2CT_x samples significantly. Most notably, some cathodic features are observed around −1.4 to −1.8 V. These features were especially clear on Ti_2CT_x (KF-HCl), indicating more significant $*CO_2$ (or related intermediates) adsorption and interaction (Salehi-Khojin et al., 2013) compared with Ti_2CT_x (HF). Additionally, the HER onset potentials on both Ti_2CT_x samples are delayed by about −0.1 to −0.2 V with reduced current density. As the electrolyte pH (~1.24) and reference electrode are unaffected by CO_2 purging (Figure S4), this HER "poisoning" effect can be attributed to $*CO_2$ (or related intermediates) adsorption that competes with *H. Such an effect is expected on transition metal surfaces that show weak *H binding strength like Ti (Huang et al., 2017; Zhang et al., 2014).

To quantify their CO_2RR activity, both Ti_2CT_x samples are subjected to chronoamperometric (constant voltage) measurement for 100 min under continuous CO_2 gas purging in a two-compartment cell

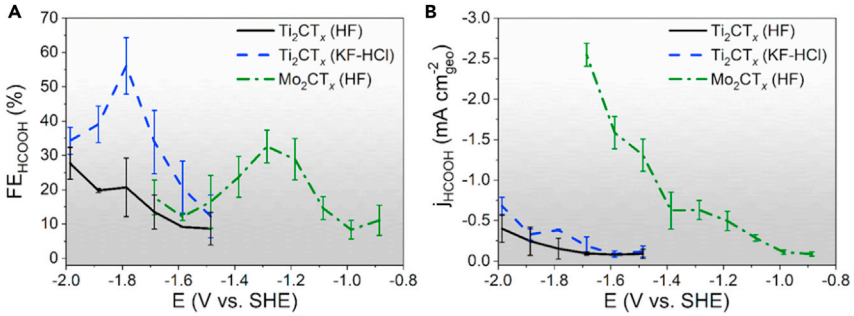

Figure 3. CO_2RR Selectivity and Activity on Ti_2CT_x and Mo_2CT_x MXenes

Comparison of (A) Faradaic efficiency and (B) partial current density normalized by geometric surface area for CO_2RR to formic acid on Ti_2CT_x and Mo_2CT_x MXenes. Error bars represent one standard deviation of three independent measurements.

(Figure S5). Both Ti_2CT_x samples retain most of their characteristic XPS peaks after CO_2RR, with slight increase in the more oxidized Ti(IV) signals due to ambient exposure during testing (Figures 2D and 2E). Online gas chromatography (GC) and nuclear magnetic resonance (NMR) were used to quantify gaseous and liquid products from CO_2RR, revealing formic acid and H_2 to be the main products on both Ti_2CT_x samples (Figures 3 and S6). It is clear from the Faradaic efficiency (FE) plot (Figure 3A) and partial current density (j) plot (Figure 3B) that Ti_2CT_x (KF-HCl) shows enhanced selectivity and turnover for CO_2RR to formic acid compared with Ti_2CT_x (HF), although the CO_2RR onset potentials are similar for both samples at −1.5 V. At a potential of −1.8 V, Ti_2CT_x (KF-HCl) displays 56.1% FE_{HCOOH} compared with 20.7% on Ti_2CT_x (HF), with a corresponding 2.5 times higher j_{HCOOH} normalized to geometric surface area. Plots of j_{HCOOH} normalized to electrochemical surface area are also shown in Figure S7 and Table S6.

To gain insight on the experimental results, we turn to DFT calculations to systematically investigate the effect of varying amounts of –F termination group on the theoretical CO_2RR overpotential on Ti_2CT_x samples. In particular, three different Ti_2CT_x structures were modeled with T_x groups comprising (1) 0.0% –F, 100.0% –O, (2) 33.3% –F, 66.7% –O, and (3) 66.7% –F, 33.3% –O (Figure S8). The T_x compositions were selected based on the range of –F termination previously studied on Ti-based MXenes (Handoko et al., 2018a). On fully –O terminated Ti_2CT_x surface, CO_2RR to formic acid is completed in four steps, including a CO_2 adsorption step, two consecutive proton-coupled electron transfer (PCET) steps, and finally an HCOOH (l) desorption step (Figure 4A). In this case, only the *COOH pathway was considered, as the alternative route through HCOO intermediate was found to be unfavorable (Figure S9), consistent with the literature (Li et al., 2017a). The $*CO_2 + H^+ + e^- \rightarrow *COOH$ step (PCET-1) is predicted to be potential limiting with a free energy change (ΔG_{elem}, at 0 V applied potential) of 0.85 eV. Hence, the theoretical CO_2RR limiting potential ($UL_{CO2} = -\Delta G_{elem}/e$) can be calculated to be −0.85 V.

Gradual –F substitution of the –O T_x group in Ti_2CT_x results in significant variation of reaction free energy (Figure 4A). Specifically, the PCET-1 potential limiting step becomes more endergonic (larger ΔG_{elem}) at a higher fraction of –F substitution. As a result, the UL_{CO2} becomes more negative at −0.89 and −1.26 V for 33.3% and 66.7% –F, respectively, possibly due to increasingly unstable *COOH conformations (Figure S8). As *HCOOH adsorption energy does not change substantially with –F substitution, we observe that the PCET-1 reaction step remains potential limiting throughout. This means that the least negative UL_{CO2} can only be achieved on fully –O terminated Ti_2CT_x. These simulation results explain the higher FE_{HCOOH} and j_{HCOOH} observed on Ti_2CT_x (KF-HCl) as it has significantly lower –F surface termination compared with Ti_2CT_x (HF).

To study if the effect of –F substitution is common to other MXenes, we expand the investigation to Mo_2CT_x. In this case, only HF etching is used, as milder KF-HCl etchant is not able to etch Mo_2Ga_2C precursor. Nonetheless, Mo_2CT_x could potentially be a better CO_2RR catalyst as it tends to have fewer –F terminations than Ti_2CT_x even when a harsher etching condition using 48% HF is used (Halim et al., 2016). The morphology of Mo_2CT_x is slightly different than Ti_2CT_x with less obvious delamination between the layers (Figure 1C), consistent with previous studies (Halim et al., 2016). XRD analyses also indicate successful etching of most Mo_2Ga_2C precursor, with a broad peak at $2\theta = 9.0°$ indicative of a (002) interlayer distance of around 9.8 Å (Figure 1D; see Figure S1 and Table S1 for characterization of precursors). XPS shows a

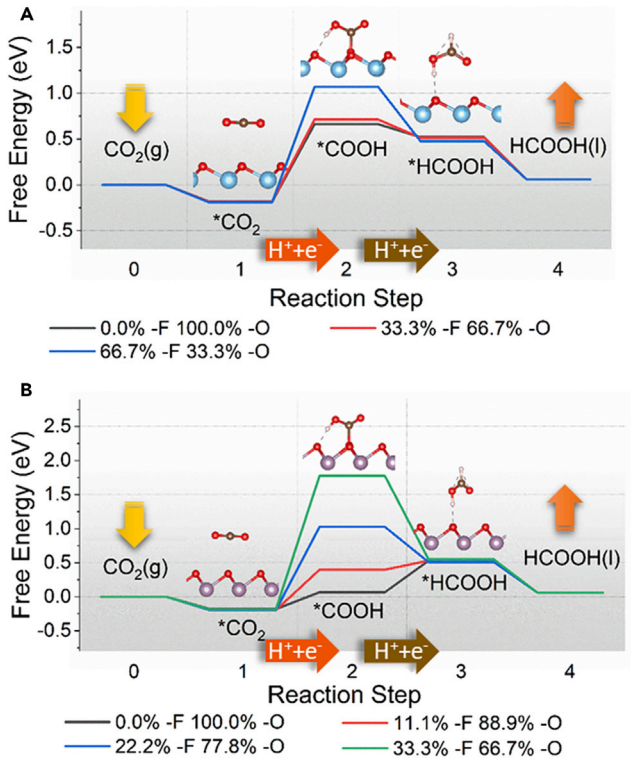

Figure 4. Density Functional Theory Calculations for CO_2RR to Formic Acid on Ti_2CT_x and Mo_2CT_x MXenes

Calculated free energy diagram at 0 V applied potential for CO_2RR to formic acid on (A) Ti_2CT_x and (B) Mo_2CT_x MXenes with varying fractions of –F and –O surface terminating groups. Blue, purple, red, brown, and white spheres represent Ti, Mo, O, C, and H atoms, respectively.

relatively large Mo-T_x/C component with no signs of Mo(VI) (Figure 2C). The F/Mo atomic ratio is estimated to be 0.03 (Table S5).

Initial LSV assessments under N_2 purging show earlier HER onset potential on Mo_2CT_x around −1.3 V (Figure S2C), which is consistent with its superior HER activity (Handoko et al., 2018a; Seh et al., 2016). However, it is unusual that Mo_2CT_x also displayed a similar HER poisoning effect under CO_2 purging since, unlike Ti, Mo should bind to *H strongly (Laursen et al., 2012). The observation of HER poisoning on both MXenes suggests that the interaction of *CO_2 or other intermediates with the T_x groups is possibly more critical than that with the base metal sites.

GC and NMR analysis during chronoamperometric measurements revealed that Mo_2CT_x starts forming formic acid at much less negative potential (−0.9 V) than both types of Ti_2CT_x (−1.5 V). This is consistent with the cathodic features observed in LSV under CO_2 purging (Figure S2C). Although the maximum FE_{HCOOH} of Mo_2CT_x (32.6% at −1.3 V, Figure 3A) is lower compared with Ti_2CT_x (KF-HCl, 56.1% at −1.8 V), the former shows significantly higher j_{HCOOH} up to −2.5 mA cm^{-2}_{geo} at less negative potentials (Figure 3B), suggesting that it is quite active in reducing CO_2 to formic acid. The stability of CO_2RR on Mo_2CT_x is assessed by conducting continuous electrolysis for 500 min. Some fluctuation in FE_{HCOOH} from 39.9% in the 100th minute to 25.7% in the 500th minute was observed (Figure S10A). We attribute the apparent FE_{HCOOH} instability to the loss of volatile acetonitrile in the electrolyte during continuous purging rather than catalyst deactivation, as no degradation of j_{HCOOH} is observed (Figure S10B). Gradual evaporation of acetonitrile would alter the electrolyte composition and increase the water proportion, leading to higher HER turnover that dominates the total current density (Figure S10B). Loss of volatile electrolyte component is a common issue for analytical electrochemical systems that require continuous sampling (Lazouski et al., 2020).

Mo_2CT_x was found to retain most of its characteristic XPS peaks after CO_2RRR as well (Figure 2F). The earlier onset and higher turnover for CO_2RR to formic acid on Mo_2CT_x is unexpected owing to its predisposition

for catalyzing HER (Seh et al., 2016; Pan, 2016; Handoko et al., 2018a). As such, Mo-based MXenes have not been considered active for CO_2RR in previous computational studies (Handoko et al., 2018b; Morales-García et al., 2018; Chen et al., 2019), with the exception of a hypothetical $Mo_3C_2(OH)_2$ structure (Li et al., 2017a).

To explain the experimental finding on Mo_2CT_x, we turn back to DFT calculations to examine CO_2RR steps on this surface. Similar to Ti_2CT_x, we construct fully –O terminated Mo_2CT_x and gradually replace the T_x with –F, but this time at lower fractions of 11.1%, 22.2%, and 33.3% (Figure S11) owing to fewer –F terminations detected experimentally. On fully –O terminated Mo_2CT_x, the reaction step *COOH + H^+ + e^- → *HCOOH (PCET-2) with ΔG_{elem} of 0.47 eV (and UL_{CO2} of −0.47 V) is found to be potential limiting. Here, –F substitution on Mo_2CT_x appears to affect CO_2RR intermediates more significantly than on Ti_2CT_x (Figure 4B). We observe on Mo_2CT_x that the ΔG_{elem} of PCET-1 increases significantly by 0.35 eV after substitution of only 11.1% of the –O termination to –F. This is in contrast to the 0.05 eV change observed on Ti_2CT_x when 33.3% of the –O T_x group is replaced by –F (Figure 4A).

More interestingly, we note that the presence of –F T_x group on Mo_2CT_x changes the potential limiting step from PCET-2 on fully –O terminated surface to PCET-1 after 11.1% –F substitution. This means that the lowest UL_{CO2} can be found at low fraction of –F substitution, between 0% and 11.1%, that equalize the ΔG_{elem} of PCET-1 and PCET-2. Quadratic functions fitting of the *COOH free energy and the respective limiting potential at different fractions of –F substitution suggest that such a minimum can be found at around 4.2% –F (Figure S12A).

One possible reason for the unique CO_2RR behavior on Ti_2CT_x and Mo_2CT_x MXenes could lie in the preference toward the *HCOOH pathway. Unlike late transition metal catalysts, where a majority of CO_2RR goes through the ubiquitous *CO intermediate (Peterson and Nørskov, 2012), the reaction path through *HCOOH intermediate is favorable on MXenes owing to the hydrogen-bond interaction between *HCOOH and the T_x groups, particularly –O (Figure S13). The preference toward the *HCOOH pathway results in non-linear scaling with *COOH in terms of their binding energies, as these two intermediates are coordinated differently on the MXene surfaces (Figure 5A). In general, *COOH binds to the –O T_x groups on MXene surfaces through C atom, whereas *HCOOH binds through the H atom (Figures S8, S11, and S13). A volcano-like plot of limiting potentials can then be constructed, with boundaries drawn to mark the neutral potential of PCET-1 (orange line) and PCET-2 (brown line) reaction steps with respect to *COOH binding energy (Figure 5B). A majority of the catalysts are governed by the PCET-1 step, where less negative UL_{CO2} is achieved at stronger *COOH binding energy, up to a point where protonation of *COOH to *HCOOH becomes difficult. It can be seen that fully –O terminated Mo_2CT_x sits atop the volcano, near to the ideal case where both PCET-1 and PCET-2 can proceed at the same limiting potential.

We also examined the HER reaction steps on both Ti_2CT_x and Mo_2CT_x surfaces at various –F substitution using DFT calculation (Figure S14). This is important as HER is the main competition to CO_2RR on these surfaces. Compared with CO_2RR, HER is a simpler reaction, which can be represented by: * + H^+ + e^- → *H → $^1/_2$ H_2 (g) + *. It is found that –F substitution generally destabilizes *H adsorption due to much weaker H-F interaction. The weaker *H results in a more negative HER limiting potential (UL_{H2}) nearly on all cases, except on Mo_2CT_x with 11.1% –F substitution where the limiting potential is close to the ideal value (−0.02 V, Figure S12B).

The difference between the limiting potentials of CO_2RR and HER (UL_{CO2}-UL_{H2}) could then be used to gauge the selectivity of the catalysts toward CO_2RR (Hong et al., 2016; Shi et al., 2014). In addition to having the least negative UL_{CO2} value, we found that –O terminated Mo_2CT_x also possesses the least negative UL_{CO2}-UL_{H2} difference of −0.1 V (Figure 5C). Quadratic functions fitting of UL_{CO2}-UL_{H2} on Mo_2CT_x identifies a minimum at 3.8% –F substitution (Figure S12B), indicating that low amounts of –F T_x presence may be beneficial to CO_2RR.

Although the UL_{CO2}-UL_{H2} values on all variants of Ti_2CT_x and Mo_2CT_x are still generally negative across all fractions of –F substitutions, we recognize that the kinetics of both HER and CO_2RR can be significantly altered by the reaction environment (König et al., 2019). In addition to the enhanced CO_2 solubility in acetonitrile, the formation of BMIM-CO_2 complex has been shown to enhance CO_2 mass transport and significantly boost CO_2RR activity (Rosen et al., 2011). Furthermore, the hydrophobic BMIM cation has been

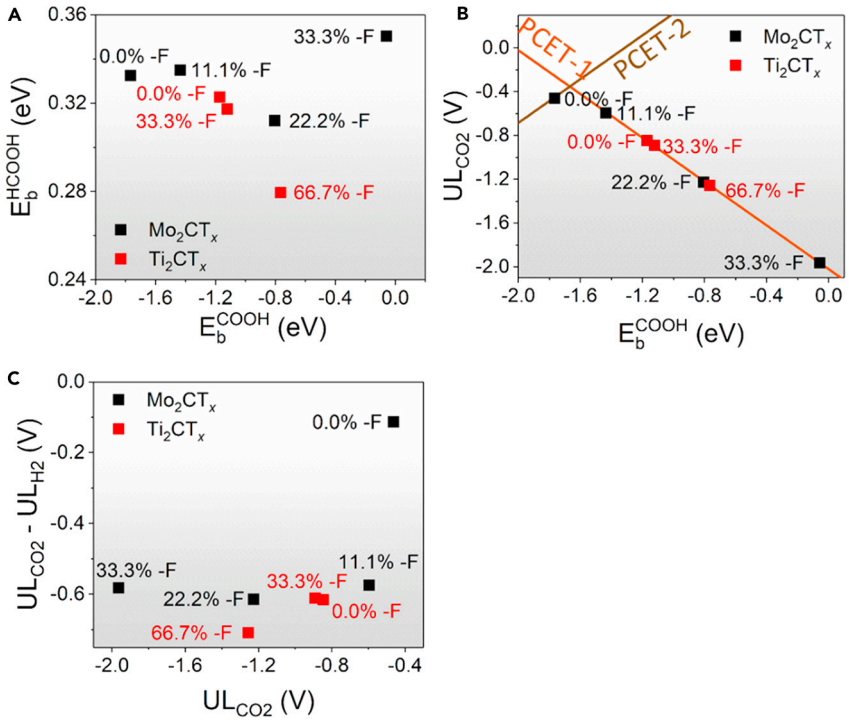

Figure 5. Relations between Binding Energies of Different CO_2RR Reaction Intermediates on Ti_2CT_x and Mo_2CT_x MXenes

(A) *HCOOH binding energy plot against *COOH binding energy showing deviation from linear scaling relations.

(B) Limiting CO_2RR potentials for elementary steps. The lines represent the calculated potential where the most negative reaction steps are neutral as a function of *COOH binding energy (PCET-1: $*CO_2 + H^+ + e^- \rightarrow *COOH$; PCET-2: $*COOH + H^+ + e^- \rightarrow *HCOOH$).

(C) Calculated UL_{CO2}-UL_{H2} plot with respect to UL_{CO2} on all variants of Ti_2CT_x and Mo_2CT_x theoretical models with different –F T_x termination fractions in this study.

proposed to populate near the catalyst surface and suppress HER upon application of CO_2RR-relevant cathodic potentials (Rosen et al., 2012).

Apart from formic acid, we also detected up to 1.1% FE of CO and trace amounts of CH_4 and multi-carbon products (Figures S15–S17). Our finding partially validates the CO_2RR route via a *HCOOH intermediate (Li et al., 2017a; Handoko et al., 2018b; Chen et al., 2019), although further optimization of MXene surface terminations (Table S7 and S8 and Figures S18–S22) is necessary to enhance the *HCOOH intermediate stability for the production of more reduced moieties like CH_4 and multi-carbon products.

DISCUSSION

In this work, we report a combined experimental and theoretical CO_2RR investigation on Ti_2CT_x and Mo_2CT_x MXenes. Formic acid is found to be the main CO_2RR product with maximum FE exceeding 56% at −1.8 V versus SHE on Ti_2CT_x (KF-HCl). In addition, CO, trace amounts of CH_4, and other multi-carbon products are also detected. More importantly, we found that the CO_2RR activity appears to be correlated with the fraction of –F and –O surface termination groups (T_x). Ti_2CT_x (HF) with large amounts of –F (less –O) shows poorer CO_2RR activity and selectivity than Ti_2CT_x (KF-HCl) with lower –F (more –O). Even higher CO_2RR activity, up to −2.5 mA cm^{-2}_{geo} is observed on Mo_2CT_x catalysts with minimal –F fraction.

DFT simulations indicate that the presence of –F destabilizes *COOH and *H, thus causing the limiting potential of both CO_2RR and HER to become more negative. An exception is found on Mo_2CT_x where small amounts of –F substitution is predicted to balance the individual limiting potentials for PCET-1 and PCET-2 steps and yield the smallest overpotential for CO_2RR to formic acid. The CO_2RR activity on MXene surfaces could be attributed to unique intermediate-T_x interaction, which results in stabilization of differently

coordinated *COOH and *HCOOH intermediates. The dissimilar binding coordination leads to deviation in linear scaling relations typically observed on late transition metal-based CO_2RR catalysts like copper.

Although the activity and selectivity toward formic acid can be further improved, this work represents an important step toward experimental demonstration of MXenes for electrocatalytic CO_2RR. The detection of trace amounts of CH_4 and other hydrocarbon products indicate that CO_2RR to more complex moieties on MXenes is possible as well. Work is ongoing to further enhance the activity and selectivity of MXene catalysts through material design strategies including surface engineering (Hart et al., 2019), doping (Yu et al., 2019; Li et al., 2018; Gao et al., 2019), and formation of composite/hybrid structures (Handoko et al., 2019; Chi et al., 2018). In addition, we believe that MXenes could be extended to other technologically important electrocatalytic reactions such as nitrogen reduction or methane oxidation, via surface/composition tailoring and catalytic reaction engineering in the future.

Limitations of the Study

This study investigates Ti- and Mo-based MXenes for CO_2RR to HCOOH and demonstrates different reaction pathways that can break the scaling relations seen in pure transition metal catalysts. However, the prevalent HER activity on MXenes requires the use of non-aqueous electrolyte, which can be challenging for reaction scale up. Gradual loss of volatile component of the non-aqueous electrolyte also causes fluctuation in the HCOOH selectivity. Further optimization of MXene surface terminations is necessary to enhance the intermediate stability for the production of more reduced moieties like CH_4 and multi-carbon products. The DFT computational methods employed here only lend insight from the thermodynamic point of view. The actual experimental result also depends on reaction kinetics that is challenging to probe in complicated systems with multiple intermediates like CO_2RR.

Resource Availability

Lead Contact

Further information and requests for resources and reagents should be directed to and will be fulfilled by the Lead Contact, Zhi Wei Seh (sehzw@imre.a-star.edu.sg).

Materials Availability

This study did not generate new unique reagents.

Data and Code Availability

This study did not generate/analyze datasets/code.

METHODS

All methods can be found in the accompanying Transparent Methods supplemental file.

SUPPLEMENTAL INFORMATION

Supplemental Information can be found online at https://doi.org/10.1016/j.isci.2020.101181.

ACKNOWLEDGMENTS

This work was supported by the Singapore National Research Foundation (NRF-NRFF2017-04). The authors thank Yury Gogotsi (Drexel University) for providing precursor materials, as well as Hwee Leng Seng (IMRE) and Teddy Salim (NTU FACTS) for XPS measurements.

AUTHOR CONTRIBUTIONS

A.D.H. and Z.W.S. conceived the idea and wrote the manuscript. A.D.H. and B.A. performed materials synthesis. A.D.H. carried out materials characterization and electrochemical testing. H.C. and Q.Z. performed DFT calculations. All the authors discussed the results and commented on the manuscript.

DECLARATION OF INTERESTS

The authors declare no competing interests.

Received: March 26, 2020
Revised: May 5, 2020
Accepted: May 15, 2020
Published: June 26, 2020

REFERENCES

Anasori, B., and Gogotsi, Y. (2019). Introduction to 2D transition metal carbides and nitrides (MXenes). In 2D Metal Carbides and Nitrides (MXenes): Structure, Properties and Applications, B. Anasori and Y. Gogotsi, eds. (Springer International Publishing), pp. 3–12.

Anasori, B., Lukatskaya, M.R., and Gogotsi, Y. (2017). 2D metal carbides and nitrides (MXenes) for energy storage. Nat. Rev. Mater. *2*, 16098.

Anasori, B., Shi, C., Moon, E.J., Xie, Y., Voigt, C.A., Kent, P.R.C., May, S.J., Billinge, S.J.L., Barsoum, M.W., and Gogotsi, Y. (2016). Control of electronic properties of 2D carbides (MXenes) by manipulating their transition metal layers. Nanoscale Horiz. *1*, 227–234.

Anasori, B., Xie, Y., Beidaghi, M., Lu, J., Hosler, B.C., Hultman, L., Kent, P.R.C., Gogotsi, Y., and Barsoum, M.W. (2015). Two-dimensional, ordered, double transition metals carbides (MXenes). ACS Nano *9*, 9507–9516.

Asadi, M., Kim, K., Liu, C., Addepalli, A.V., Abbasi, P., Yasaei, P., Phillips, P., Behranginia, A., Cerrato, J.M., Haasch, R., et al. (2016). Nanostructured transition metal dichalcogenide electrocatalysts for CO_2 reduction in ionic liquid. Science *353*, 467–470.

Cao, S., Shen, B., Tong, T., Fu, J., and Yu, J. (2018). 2D/2D heterojunction of ultrathin MXene/Bi_2WO_6 nanosheets for improved photocatalytic CO_2 reduction. Adv. Funct. Mater. *28*, 1800136.

Chen, H., Handoko, A.D., Xiao, J., Feng, X., Fan, Y., Wang, T., Legut, D., Seh, Z.W., and Zhang, Q. (2019). Catalytic effect on CO_2 electroreduction by hydroxyl terminated two-dimensional MXenes. ACS Appl. Mater. Interfaces *11*, 36571–36579.

Chi, C., Xiuqiang, X., Babak, A., Asya, S., Taron, M., Mengqiang, Z., Patrick, U., Ling, M., Jianjun, J., and Yury, G. (2018). MoS_2-on-MXene heterostructures as highly reversible anode materials for lithium-ion batteries. Angew. Chem. Int. Ed. *57*, 1846–1850.

De Luna, P., Hahn, C., Higgins, D., Jaffer, S.A., Jaramillo, T.F., and Sargent, E.H. (2019). What would it take for renewably powered electrosynthesis to displace petrochemical processes? Science *364*, eaav3506.

Deysher, G., Shuck, C.E., Hantanasirisakul, K., Frey, N.C., Foucher, A.C., Maleski, K., Sarycheva, A., Shenoy, V.B., Stach, E.A., Anasori, B., and Gogotsi, Y. (2020). Synthesis of Mo_4VAlC_4 MAX phase and two-dimensional Mo_4VC_4 MXene with five atomic layers of transition metals. ACS Nano *14*, 204–217.

Gao, Z.-W., Zheng, W., and Lee, L.Y.S. (2019). Highly enhanced pseudocapacitive performance of vanadium-doped MXenes in neutral electrolytes. Small *15*, 1902649.

Gennaro, A., Isse, A.A., and Vianello, E. (1990). Solubility and electrochemical determination of CO_2 in some dipolar aprotic solvents. J. Electroanal. Chem. Interfacial Electrochem. *289*, 203–215.

Halim, J., Kota, S., Lukatskaya, M.R., Naguib, M., Zhao, M.-Q., Moon, E.J., Pitock, J., Nanda, J., May, S.J., Gogotsi, Y., and Barsoum, M.W. (2016). Synthesis and characterization of 2D molybdenum carbide (MXene). Adv. Funct. Mater. *26*, 3118–3127.

Handoko, A.D., Fredrickson, K.D., Anasori, B., Convey, K.W., Johnson, L.R., Gogotsi, Y., Vojvodic, A., and Seh, Z.W. (2018a). Tuning the basal plane functionalization of two-dimensional metal carbides (MXenes) to control hydrogen evolution activity. ACS Appl. Energy Mater. *1*, 173–180.

Handoko, A.D., Khoo, K.H., Tan, T.L., Jin, H., and Seh, Z.W. (2018b). Establishing new scaling relations on two-dimensional MXenes for CO_2 electroreduction. J. Mater. Chem. A *6*, 21885–21890.

Handoko, A.D., Ong, C.W., Huang, Y., Lee, Z.G., Lin, L., Panetti, G.B., and Yeo, B.S. (2016). Mechanistic insights into the selective electroreduction of carbon dioxide to ethylene on Cu_2O-derived copper catalysts. J. Phys. Chem. C *120*, 20058–20067.

Handoko, A.D., Steinmann, S.N., and Seh, Z.W. (2019). Theory-guided materials design: two-dimensional MXenes in electro- and photocatalysis. Nanoscale Horiz. *4*, 809–827.

Handoko, A.D., Wei, F., Jenndy, Yeo, B.S., and Seh, Z.W. (2018c). Understanding heterogeneous electrocatalytic carbon dioxide reduction through operando techniques. Nat. Catal. *1*, 922–934.

Hart, J.L., Hantanasirisakul, K., Lang, A.C., Anasori, B., Pinto, D., Pivak, Y., van Omme, J.T., May, S.J., Gogotsi, Y., and Taheri, M.L. (2019). Control of MXenes' electronic properties through termination and intercalation. Nat. Commun. *10*, 522.

Higgins, D., Hahn, C., Xiang, C., Jaramillo, T.F., and Weber, A.Z. (2019). Gas-Diffusion electrodes for carbon dioxide reduction: a new paradigm. ACS Energy Lett. *4*, 317–324.

Hong, X., Chan, K., Tsai, C., and Nørskov, J.K. (2016). How doped MoS_2 breaks transition-metal scaling relations for CO_2 electrochemical reduction. ACS Catal. *6*, 4428–4437.

Hope, M.A., Forse, A.C., Griffith, K.J., Lukatskaya, M.R., Ghidiu, M., Gogotsi, Y., and Grey, C.P. (2016). NMR reveals the surface functionalisation of Ti_3C_2 MXene. Phys. Chem. Chem. Phys. *18*, 5099–5102.

Hori, Y. (2008). Electrochemical CO_2 reduction on metal electrodes. In Modern Aspects of Electrochemistry, C.G. Vayenas, R.E. White, and M.E. Gamboa-Aldeco, eds. (Springer), pp. 102–115.

Huang, Y., Handoko, A.D., Hirunsit, P., and Yeo, B.S. (2017). Electrochemical reduction of CO_2 using copper single-crystal surfaces: effects of CO* coverage on the selective formation of ethylene. ACS Catal. *7*, 1749–1756.

Jouny, M., Luc, W., and Jiao, F. (2018). General techno-economic analysis of CO_2 electrolysis systems. Ind. Eng. Chem. Res. *57*, 2165–2177.

König, M., Vaes, J., Klemm, E., and Pant, D. (2019). Solvents and supporting electrolytes in the electrocatalytic reduction of CO_2. iScience *19*, 135–160.

Laursen, A.B., Varela, A.S., Dionigi, F., Fanchiu, H., Miller, C., Trinhammer, O.L., Rossmeisl, J., and Dahl, S. (2012). Electrochemical hydrogen evolution: sabatier's principle and the volcano plot. J. Chem. Educ. *89*, 1595–1599.

Lazouski, N., Chung, M., Williams, K., Gala, M.L., and Manthiram, K. (2020). Non-aqueous gas diffusion electrodes for rapid ammonia synthesis from nitrogen and water-splitting-derived hydrogen. Nat. Catal. https://doi.org/10.1038/s41929-020-0455-8.

Li, N., Chen, X., Ong, W.-J., MacFarlane, D.R., Zhao, X., Cheetham, A.K., and Sun, C. (2017a). Understanding of electrochemical mechanisms for CO_2 capture and conversion into hydrocarbon fuels in transition-metal carbides (MXenes). ACS Nano *11*, 10825–10833.

Li, P., Zhu, J., Handoko, A.D., Zhang, R., Wang, H., Legut, D., Wen, X., Fu, Z., Seh, Z.W., and Zhang, Q. (2018). High-throughput theoretical optimization of the hydrogen evolution reaction on MXenes by transition metal modification. J. Mater. Chem. A *6*, 4271–4278.

Li, Y., Cui, F., Ross, M.B., Kim, D., Sun, Y., and Yang, P. (2017b). Structure-sensitive CO_2 electroreduction to hydrocarbons on ultrathin 5-fold twinned copper nanowires. Nano Lett. *17*, 1312–1317.

Liu, X., Xiao, J., Peng, H., Hong, X., Chan, K., and Nørskov, J.K. (2017). Understanding trends in electrochemical carbon dioxide reduction rates. Nat. Commun. *8*, 15438.

Matsubara, Y., Grills, D.C., and Kuwahara, Y. (2015). Thermodynamic aspects of electrocatalytic CO_2 reduction in acetonitrile and with an ionic liquid as solvent or electrolyte. ACS Catal. *5*, 6440–6452.

Mistry, H., Varela, A.S., Bonifacio, C.S., Zegkinoglou, I., Sinev, I., Choi, Y.W., Kisslinger, K., Stach, E.A., Yang, J.C., Strasser, P., and Cuenya, B.R. (2016). Highly selective plasma-

activated copper catalysts for carbon dioxide reduction to ethylene. Nat. Commun. *7*, 12123.

Morales-García, Á., Fernández-Fernández, A., Viñes, F., and Illas, F. (2018). CO_2 abatement using two-dimensional MXene carbides. J. Mater. Chem. A *6*, 3381–3385.

Naguib, M., Mashtalir, O., Carle, J., Presser, V., Lu, J., Hultman, L., Gogotsi, Y., and Barsoum, M.W. (2012). Two-Dimensional Transition Metal Carbides. ACS Nano *6*, 1322–1331.

Obama, B. (2017). The irreversible momentum of clean energy. Science *355*, 126–129.

Pan, H. (2016). Ultra-high electrochemical catalytic activity of MXenes. Sci. Rep. *6*, 32531.

Peterson, A.A., and Nørskov, J.K. (2012). Activity descriptors for CO_2 electroreduction to methane on transition-metal catalysts. J. Phys. Chem. Lett. *3*, 251–258.

Ren, D., Wong, N.T., Handoko, A.D., Huang, Y., and Yeo, B.S. (2016). Mechanistic insights into the enhanced activity and stability of agglomerated Cu nanocrystals for the electrochemical reduction of carbon dioxide to n-propanol. J. Phys. Chem. Lett. *7*, 20–24.

Rosen, B.A., Haan, J.L., Mukherjee, P., Braunschweig, B., Zhu, W., Salehi-Khojin, A., Dlott, D.D., and Masel, R.I. (2012). In situ spectroscopic examination of a low overpotential pathway for carbon dioxide conversion to carbon monoxide. J. Phys. Chem. C *116*, 15307–15312.

Rosen, B.A., Salehi-Khojin, A., Thorson, M.R., Zhu, W., Whipple, D.T., Kenis, P.J.A., and Masel, R.I. (2011). Ionic liquid–mediated selective conversion of CO_2 to CO at low overpotentials. Science *334*, 643–644.

Saberi Safaei, T., Mepham, A., Zheng, X., Pang, Y., Dinh, C.-T., Liu, M., Sinton, D., Kelley, S.O., and Sargent, E.H. (2016). High-density nanosharp microstructures enable efficient CO_2 electroreduction. Nano Lett. *16*, 7224–7228.

Salehi-Khojin, A., Jhong, H.-R.M., Rosen, B.A., Zhu, W., Ma, S., Kenis, P.J.A., and Masel, R.I. (2013). Nanoparticle silver catalysts that show enhanced activity for carbon dioxide electrolysis. J. Phys. Chem. C *117*, 1627–1632.

Seh, Z.W., Fredrickson, K.D., Anasori, B., Kibsgaard, J., Strickler, A.L., Lukatskaya, M.R., Gogotsi, Y., Jaramillo, T.F., and Vojvodic, A. (2016). Two-dimensional molybdenum carbide (MXene) as an efficient electrocatalyst for hydrogen evolution. ACS Energy Lett. *1*, 589–594.

Seh, Z.W., Kibsgaard, J., Dickens, C.F., Chorkendorff, I., Nørskov, J.K., and Jaramillo, T.F. (2017). Combining theory and experiment in electrocatalysis: insights into materials design. Science *355*, eaad4998.

Shi, C., Hansen, H.A., Lausche, A.C., and Norskov, J.K. (2014). Trends in electrochemical CO_2 reduction activity for open and close-packed metal surfaces. Phys. Chem. Chem. Phys. *16*, 4720–4727.

Walsh, B., Ciais, P., Janssens, I.A., Peñuelas, J., Riahi, K., Rydzak, F., van Vuuren, D.P., and Obersteiner, M. (2017). Pathways for balancing CO_2 emissions and sinks. Nat. Commun. *8*, 14856.

Yang, J., Naguib, M., Ghidiu, M., Pan, L.-M., Gu, J., Nanda, J., Halim, J., Gogotsi, Y., and Barsoum, M.W. (2016). Two-dimensional Nb-based M_4C_3 solid solutions (MXenes). J. Am. Ceram. Soc. *99*, 660–666.

Ye, M., Wang, X., Liu, E., Ye, J., and Wang, D. (2018). Boosting the photocatalytic activity of P25 for carbon dioxide reduction by using a surface-alkalinized titanium carbide MXene as cocatalyst. ChemSusChem *11*, 1606–1611.

Yu, L., Fan, Z., Shao, Y., Tian, Z., Sun, J., and Liu, Z. (2019). Versatile N-doped MXene ink for printed electrochemical energy storage application. Adv. Energy Mater. *9*, 1901839.

Zhang, C.J., Pinilla, S., McEvoy, N., Cullen, C.P., Anasori, B., Long, E., Park, S.-H., Seral-Ascaso, A., Shmeliov, A., Krishnan, D., et al. (2017a). Oxidation stability of colloidal two-dimensional titanium carbides (MXenes). Chem. Mater. *29*, 4848–4856.

Zhang, X., Zhang, Z., Li, J., Zhao, X., Wu, D., and Zhou, Z. (2017b). Ti_2CO_2 MXene: a highly active and selective photocatalyst for CO_2 reduction. J. Mater. Chem. A *5*, 12899–12903.

Zhang, Y.-J., Sethuraman, V., Michalsky, R., and Peterson, A.A. (2014). Competition between CO_2 reduction and H_2 evolution on transition-metal electrocatalysts. ACS Catal. *4*, 3742–3748.

iScience, Volume *23*

Supplemental Information

Two-Dimensional Titanium and Molybdenum Carbide MXenes as Electrocatalysts for CO_2 Reduction

Albertus D. Handoko, Hetian Chen, Yanwei Lum, Qianfan Zhang, Babak Anasori, and Zhi Wei Seh

Supplemental figures and data

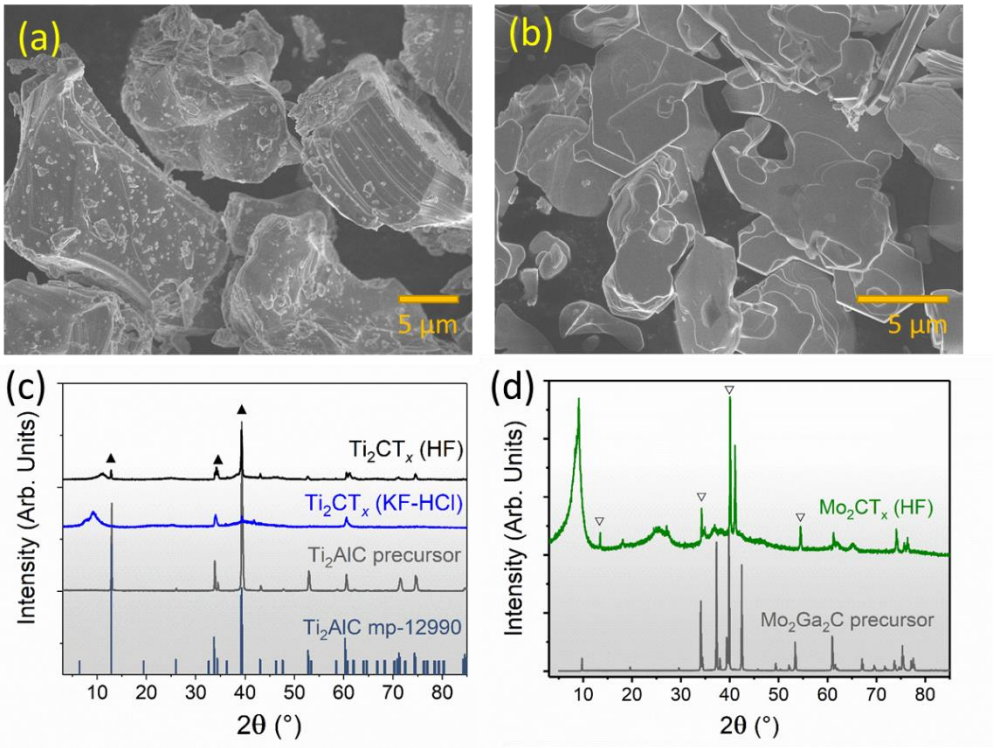

Figure S1: Characterisation of the precursor phases before etching: (a, c) Ti_2AlC and (b, d) Mo_2Ga_2C. The resulting MXene phase is inserted in (c and d) to check for presence of precursor phase. A standard Ti_2AlC pattern generated from CIF file from materials project (structure mp-12990) is included in (c). Small amounts of Ti_2AlC (▲) and Mo_2Ga_2C (▽) precursor residues were observed. Related to Figure 1.

Table S1: XPS analysis to quantify precursor residues. Related to Figure 1.

Element	Ti_2CT_x (HF)
Ti	50.24%
C	8.49%
O	16.43%
F	17.81%
Al	7.03%

Element	Ti_2CT_x (KF-HCl)
Ti	40.91%
C	24.11%
O	18.18%
F	16.79%
Al	N. Q.

Element	Mo_2CT_x (HF)
Mo	69.53%
C	7.61%
O	15.69%
F	2.90%
Ga	4.28%

N.Q.: not quantified due to very low signal to noise ratio.

Table S2: Oxidation state fraction of "M" elements in M_2CT_x MXenes. Related to Figure 2.

	Ti_2CT_x (HF)		Ti_2CT_x (KF-HCl)		Mo_2CT_x (HF)	
	pre-CO_2RR	post-CO_2RR	pre-CO_2RR	post-CO_2RR	pre-CO_2RR	post-CO_2RR
M-T_x/C (MXene)	37.7%	27.3%	26.8%	19.6%	49.4%	21.5%
Ti(II)	55.9%	47.6%	46.6%	28.0%	n.a.	n.a.
Ti(IV)	6.4%	25.1%	26.6%	52.4%	n.a.	n.a.
Mo(V)	n.a.	n.a.	n.a.	n.a.	50.6%	48.6%
Mo(VI)	n.a.	n.a.	n.a.	n.a.	n.a.	29.9%

Table S3: XPS details for Ti_2CT_x (HF) before CO_2RR. Related to Figure 2.

Element	Samples						Average	Stdev
	1	2	3	4	5	6		
Ti	44.77%	37.15%	48.98%	39.04%	39.49%	50.17%	43.27%	5.52%
C	10.98%	3.46%	14.78%	9.96%	10.65%	11.04%	10.15%	3.69%
O	21.24%	39.24%	25.58%	37.15%	35.17%	27.43%	30.97%	7.22%
F	23.01%	20.16%	10.66%	13.85%	14.69%	11.35%	15.62%	4.94%

Average F/Ti = 0.36

Table S4: XPS details for Ti_2CT_x (KF-HCl) before CO_2RR. Related to Figure 2.

Element	Samples					Average	Stdev
	1	2	3	4	5		
Ti	36.00%	35.04%	33.22%	28.70%	31.51%	32.89%	2.91%
C	26.97%	26.66%	26.56%	33.41%	29.39%	28.60%	2.93%
O	30.97%	31.09%	33.87%	30.81%	31.00%	31.55%	1.30%
F	6.07%	7.21%	6.34%	7.09%	8.09%	6.96%	0.80%

Average F/Ti = 0.21

Table S5: XPS details for Mo_2CT_x (HF) before CO_2RR. Related to Figure 2.

Element	Samples					Average	Stdev
	1	2	3	4	5		
Mo	54.82%	72.64%	64.47%	65.76%	66.98%	64.93%	6.45%
C	12.69%	7.95%	9.61%	5.71%	6.11%	8.41%	2.85%
O	29.83%	16.39%	24.11%	27.08%	25.71%	24.63%	5.06%
F	2.65%	3.03%	1.81%	1.44%	1.20%	2.03%	0.79%

Average F/Mo = 0.03

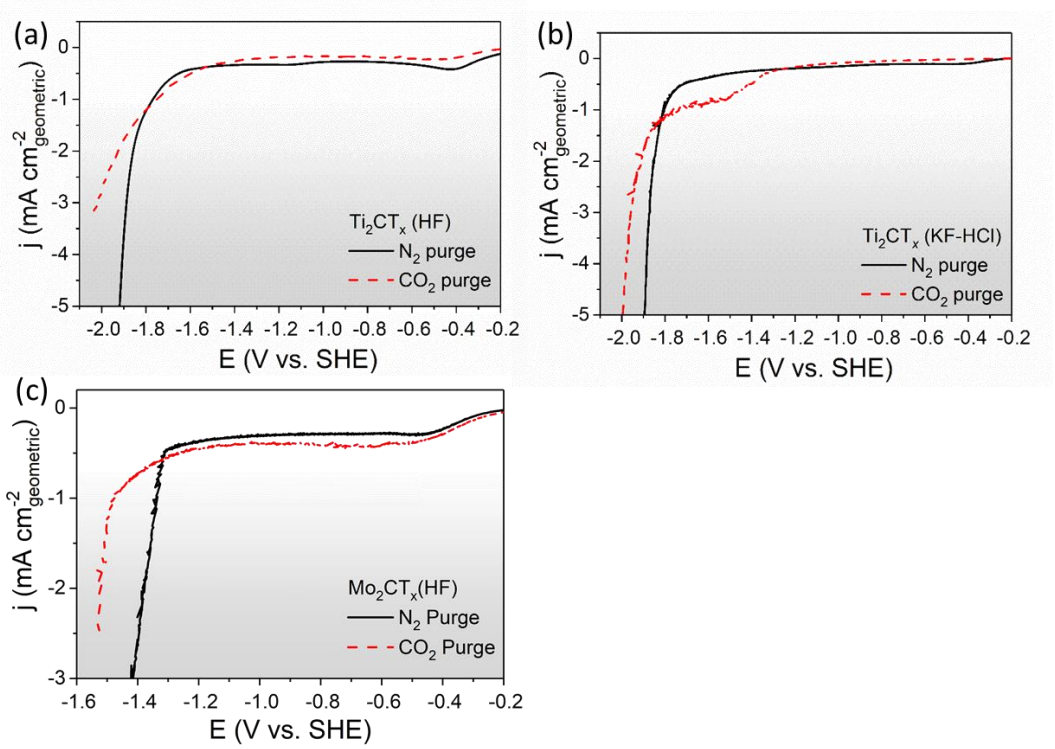

Figure S2: Linear scanning voltammetry (LSV) scans of MXenes in the presence and absence of CO_2: (a) Ti_2CT_x (HF), (b) Ti_2CT_x (KF-HCl), and (c) Mo_2CT_x (HF). Electrolyte: acetonitrile-H_2O-$BMIMBF_4$ mixture. Gas purging: N_2 and CO_2 purged as marked. iR drop is compensated via positive feedback correction at 85% of estimated R_u obtained by electrochemical impedance spectroscopy (EIS) measurement. Related to Figure 3.

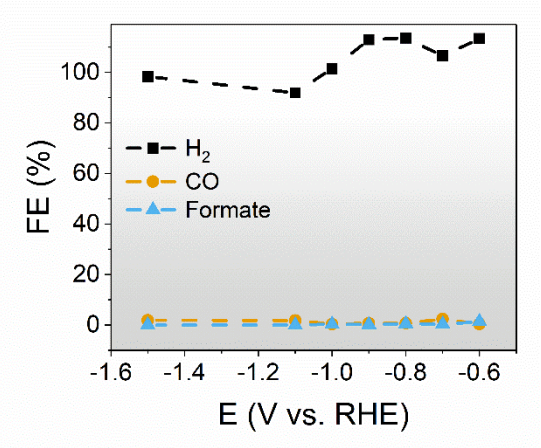

Figure S3: CO_2RR on Ti_2CT_x (KF-HCl) in 0.1 M $KHCO_3$ aqueous electrolyte. All conditions identical except that the electrolyte in both anodic and cathodic compartments is replaced with CO_2 purged 0.1 M $KHCO_3$ aqueous solution. Related to Figure 3.

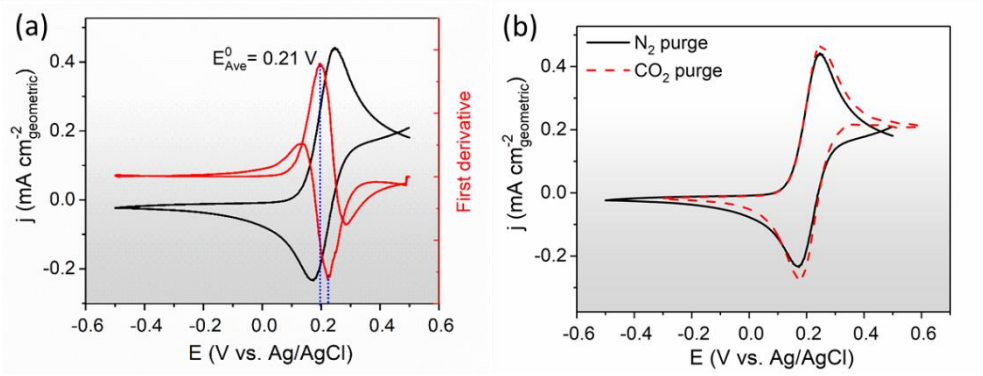

Figure S4: Cyclic voltammetry (CV) of glassy carbon electrode in acetonitrile-H_2O-BMIMBF$_4$ electrolyte with 5 mM of ferrocene. (b) Comparison of N_2 and CO_2 purged electrolyte. The reference electrode used in this work is calibrated by conducting CV scans in acetonitrile-H_2O-BMIMBF$_4$ electrolyte mixture in the presence of 5 mM ferrocene. Average of anodic going and cathodic going first derivative of the CV cycle is determined to be 0.21 V. Fc/Fc$^+$ redox potential in acetonitrile solution is taken at 0.624 V vs. SHE,(Pavlishchuk and Addison, 2000) thus the conversion value of Ag/AgCl in acetonitrile-H_2O-BMIMBF$_4$ electrolyte mixture is determined to be 0.414 V. We further determine that the Fc/Fc$^+$ reaction and reference electrode is unchanged in presence of CO_2 purging, indicating that the bicarbonate buffer system is insignificant in our electrolyte system. Related to Figure 3.

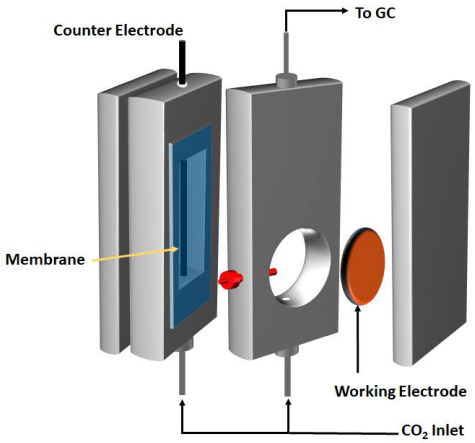

Figure S5: Schematic of two-compartment electrochemical cell used for CO_2RR in this work. Related to Figure 3.

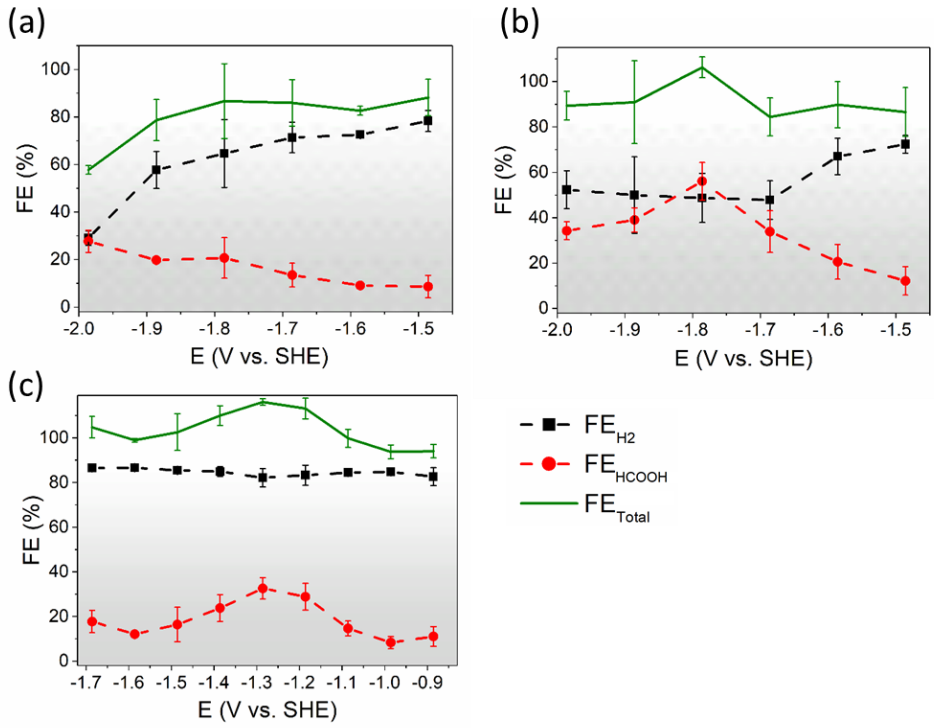

Figure S6: FE of CO_2RR major products for (a) Ti_2CT_x (HF); (b) Ti_2CT_x (KF-HCl); and (c) Mo_2CT_x (HF). Related to Figure 3.

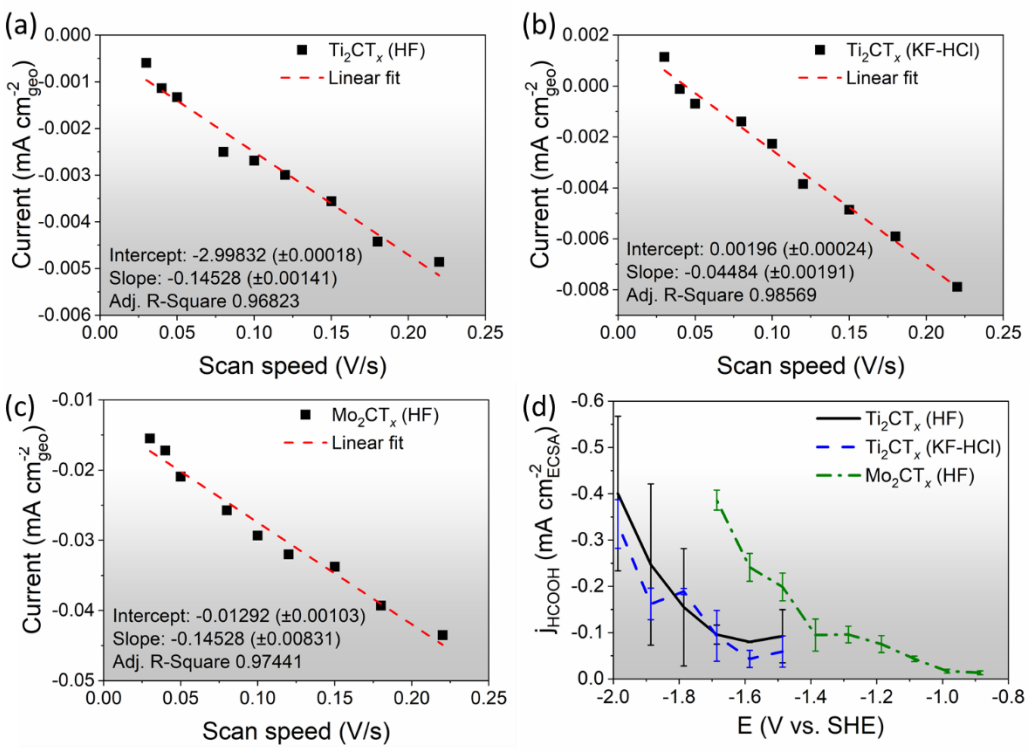

Figure S7: Plot of geometric current density in consecutive CV measurements at varying scan speeds to estimate double layer capacitance in (a) Ti_2CT_x (HF), (b) Ti_2CT_x (KF-HCl), and (c) Mo_2CT_x (HF). (d) Relative electrochemical surface area (ECSA) normalised partial current density of CO_2RR to formic acid on Ti_2CT_x and Mo_2CT_x MXenes. Error bars represent one standard deviation of three independent measurements. Related to Figure 3.

Table S6: Tabulation of measured double layer capacitance value and the respective normalised surface area of MXenes. Related to Figure 3.

	Ti_2CT_x (HF)	Ti_2CT_x (KF-HCl)	Mo_2CT_x (HF)
Capacitance value (μF)	29.2	59.5	192.8
Normalised	1	2.03	6.59

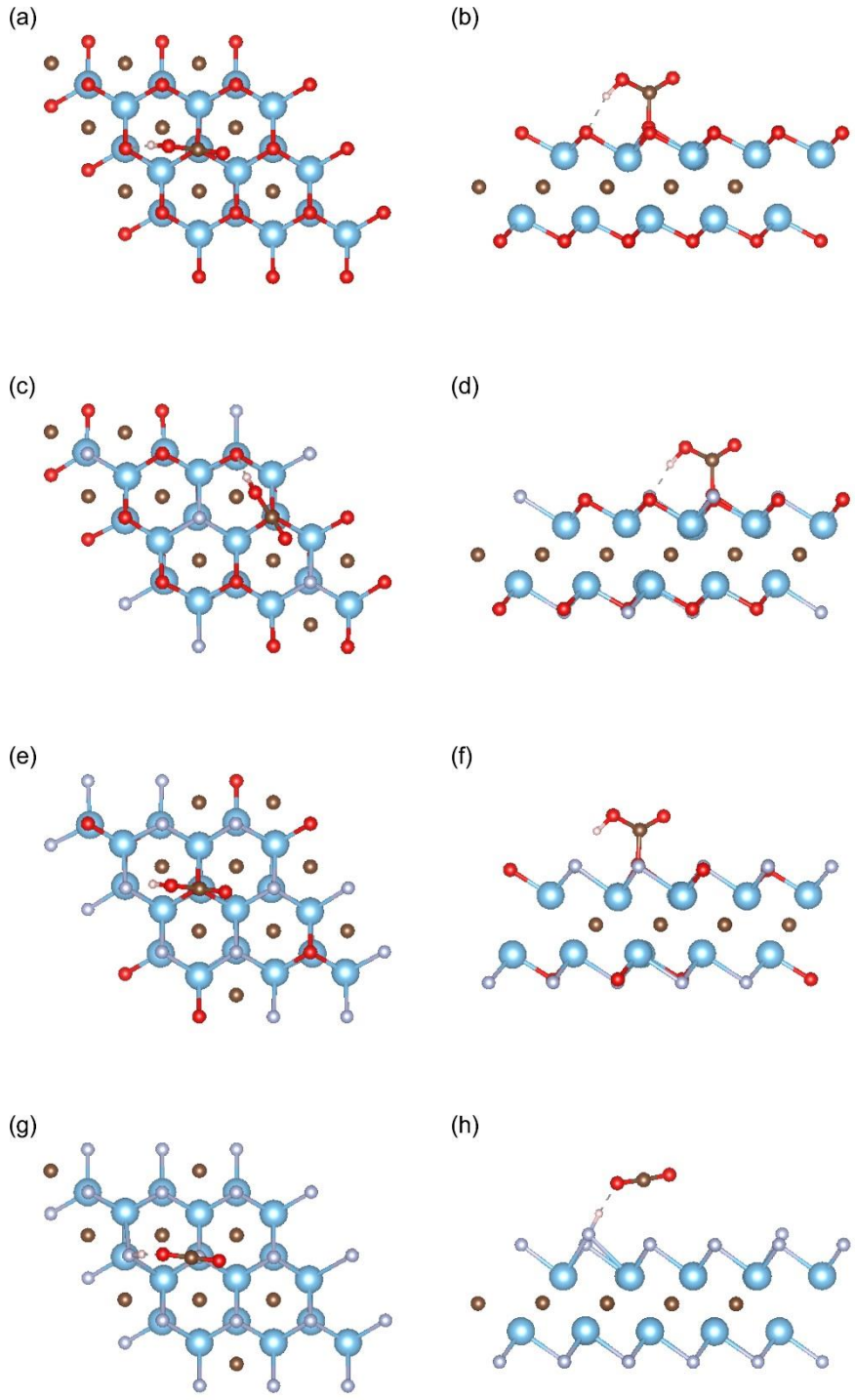

Figure S8: Top and side view of *COOH intermediate conformation on Ti_2CT_x surface with different T_x groups: (a-b) fully –O terminated, (c-d) 33.3% –F 66.7% –O terminated, (e-f) 66.7% –F 33.3% –O terminated, (g-h) fully –F terminated. Related to Figure 4.

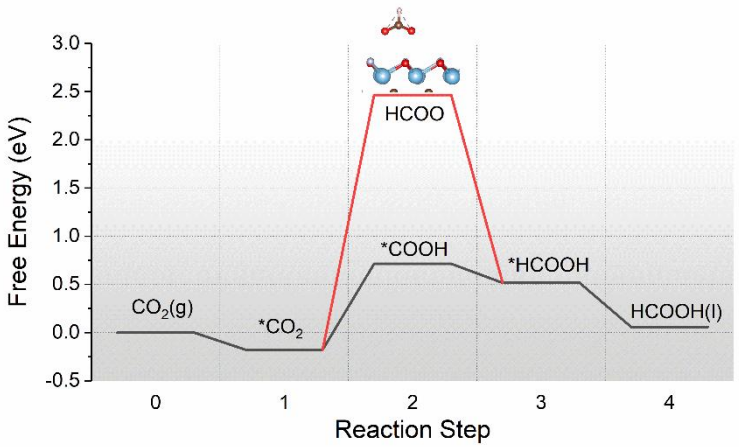

Figure S9: Calculated free energy diagram at 0 V applied potential for CO_2RR to formic acid through an alternative HCOO pathway compared to the *COOH pathway on Ti_2CT_x (33.3% –F, 66.7% –O). Related to Figure 4.

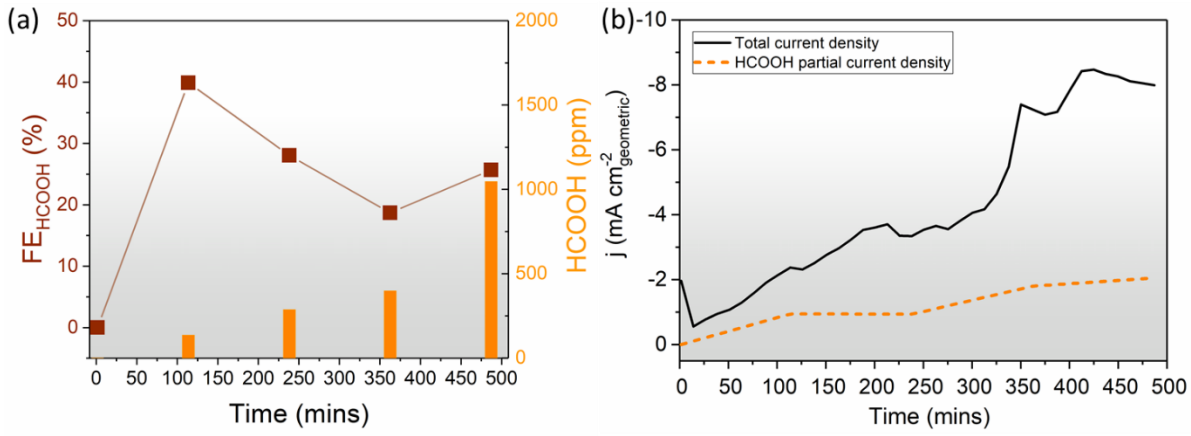

Figure S10: (a) Periodic sampling of HCOOH concentration during 500 mins CO_2RR on Mo_2CT_x showing the Faradaic efficiency (squares, left axis) and the measured HCOOH concentration (orange bars, right axis), as well as (b) total current density and HCOOH partial current density. The apparent Faradaic efficiency instability is attributed to change in electrolyte composition due to loss of acetonitrile, resulting in a significant increase in hydrogen evolution activity while maintaining CO_2RR to HCOOH. This is reflected in the increased total current density and relatively stable HCOOH partial current density. Related to Figure 3.

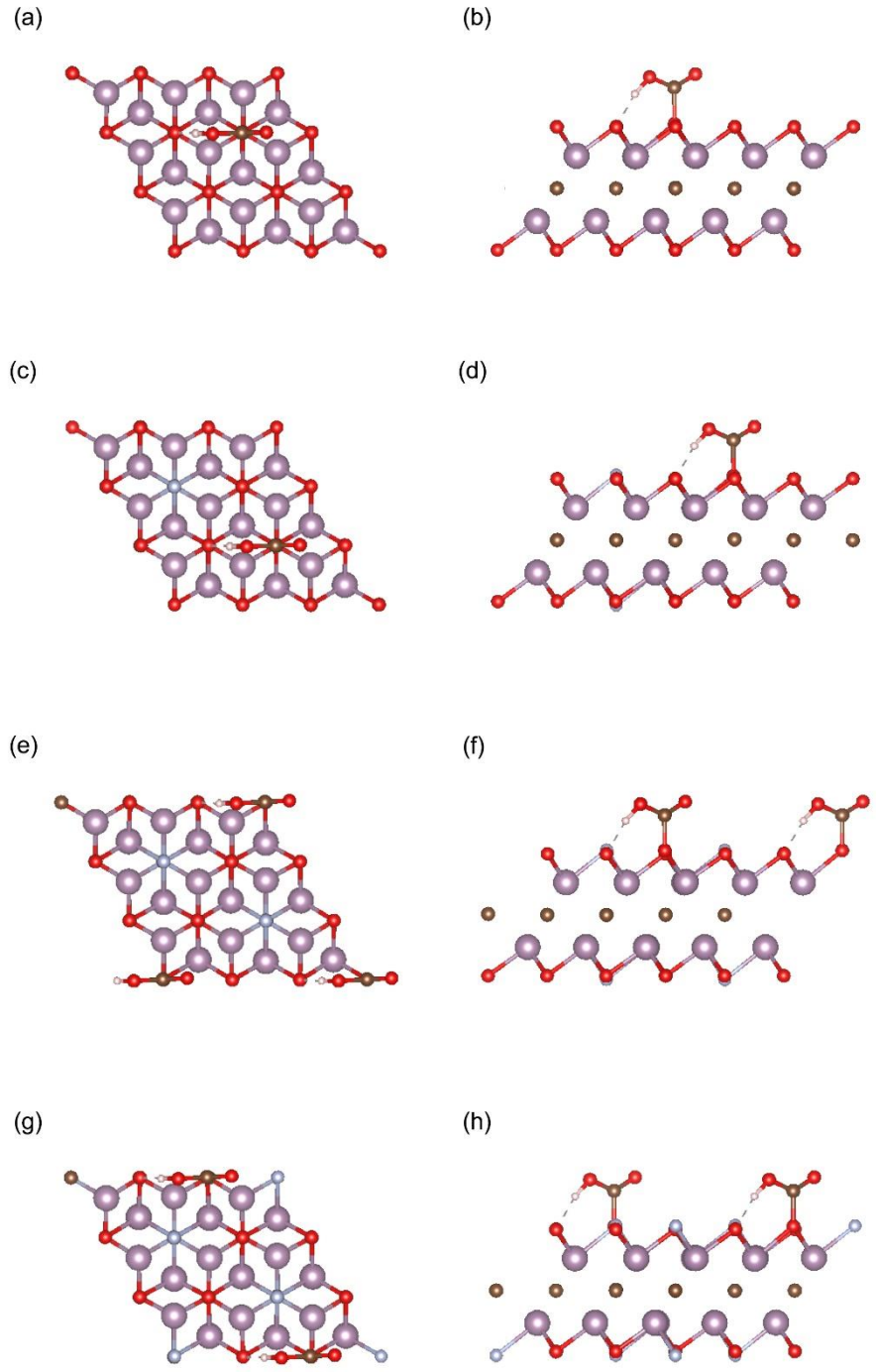

Figure S11: Top and side view of *COOH intermediate conformation on Mo_2CT_x surface with different T_x groups: (a-b) fully –O terminated, (c-d) 11.1% –F 88.9% –O terminated, (e-f) 22.2% –F 77.8% –O terminated, and (g-h) 33.3% –F 66.7% –O terminated. Related to Figure 4.

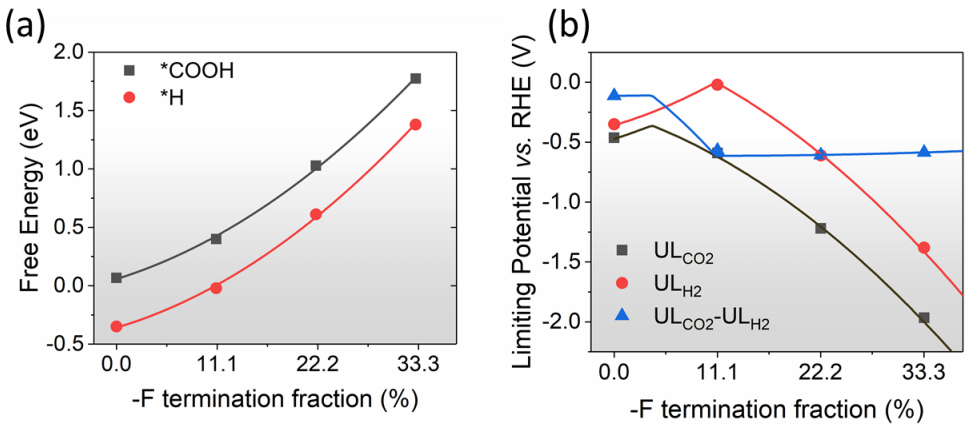

Figure S12: Fitting function diagram of the (a) *COOH and *H free energy and (b) the corresponding limiting potentials for CO_2RR, HER and the difference between the two (UL_{CO2}-UL_{H2}) on Mo_2CT_x MXene at varying –F T_x fraction. Related to Figure 5.

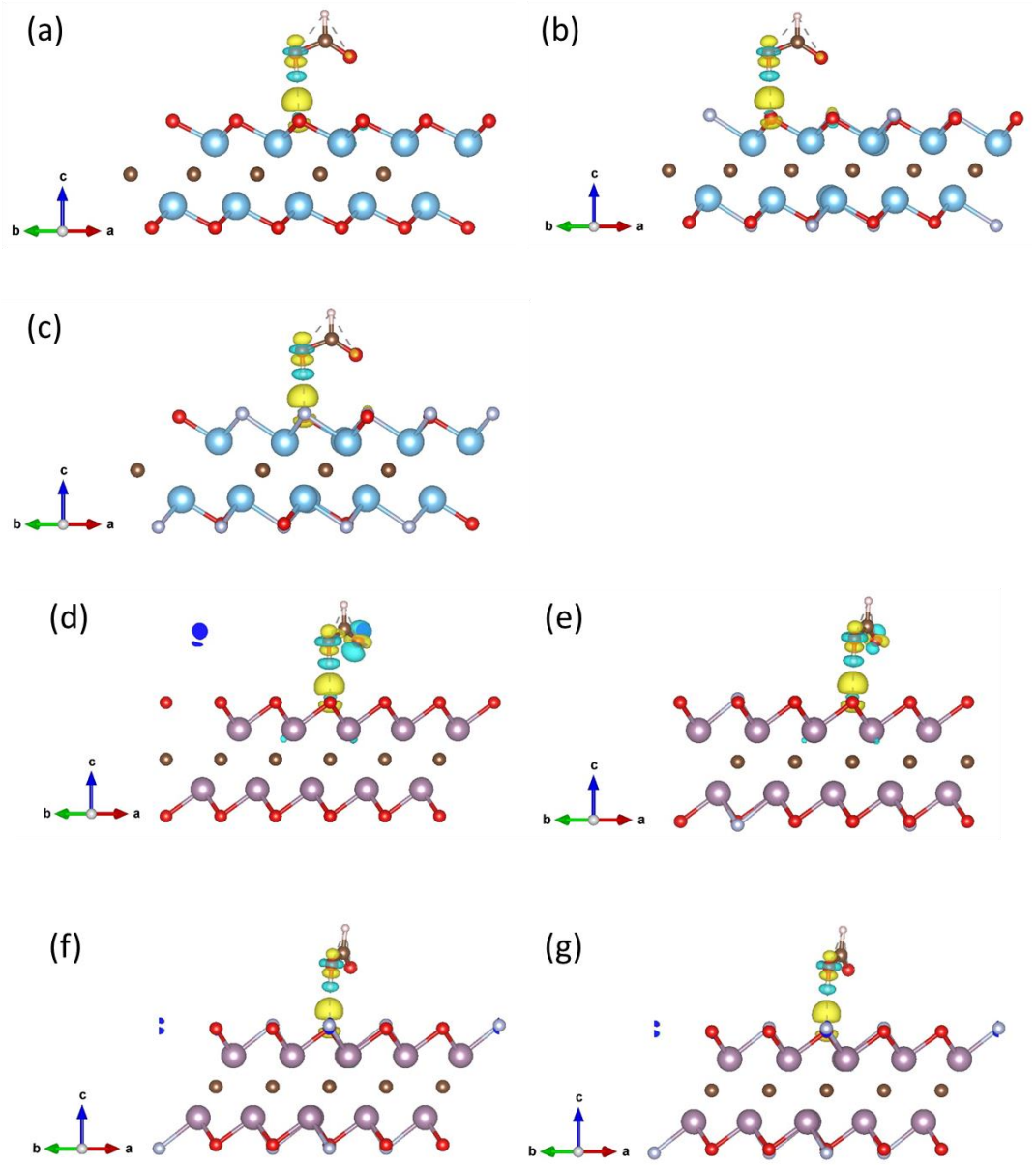

Figure S13: Charge deformation density of adsorbed *HCOOH intermediates on Ti_2CT_x (a) fully –O terminated, (b) 33.3% –F 66.7% –O terminated, (c) 66.7% –F 33.3% –O terminated, and Mo_2CT_x (d) fully –O terminated, (e) 11.1% –F 88.9% –O terminated, (f) 22.2% –F 77.8% –O terminated, and (g) 33.3% –F 66.7% –O terminated. Iso-surfaces drawn represent 0.002 e $bohr^{-3}$. Charges flow out from blue areas to yellow areas. Related to Figure 5.

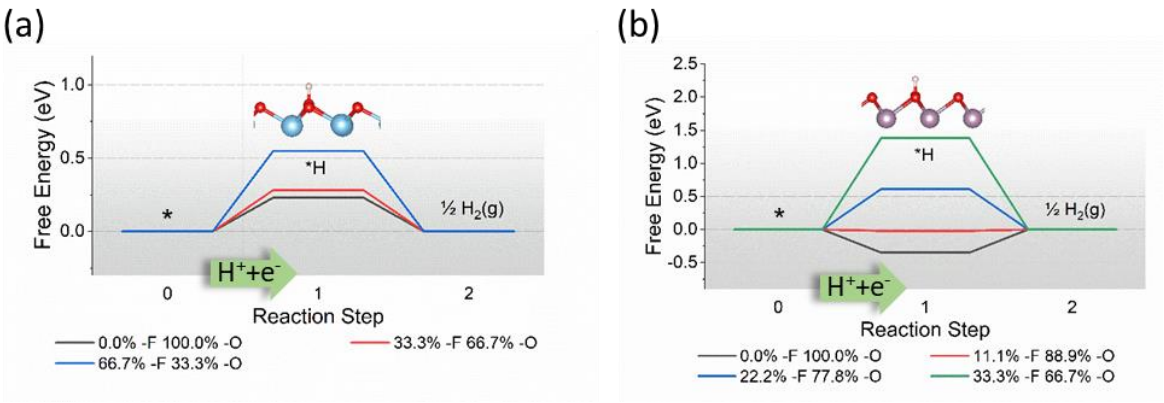

Figure S14: Calculated free energy diagram of HER at 0 V applied potential on (a) Ti_2CT_x and (b) Mo_2CT_x at varying –F T_x fraction. Related to Figure 5.

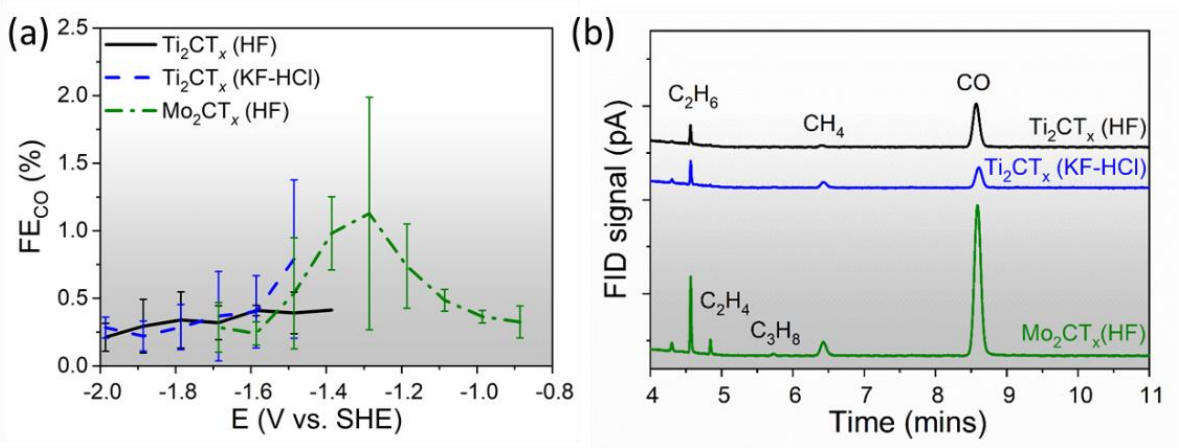

Figure S15: (a) FE data for minor product (CO) and (b) representative gas chromatogram FID of Ti_2CT_x and Mo_2CT_x at -1.5 V showing trace levels of CO and CH_4. Other products C_2H_4, C_2H_6 and C_3H_8 are not quantified due to low amounts. Related to Figure 3.

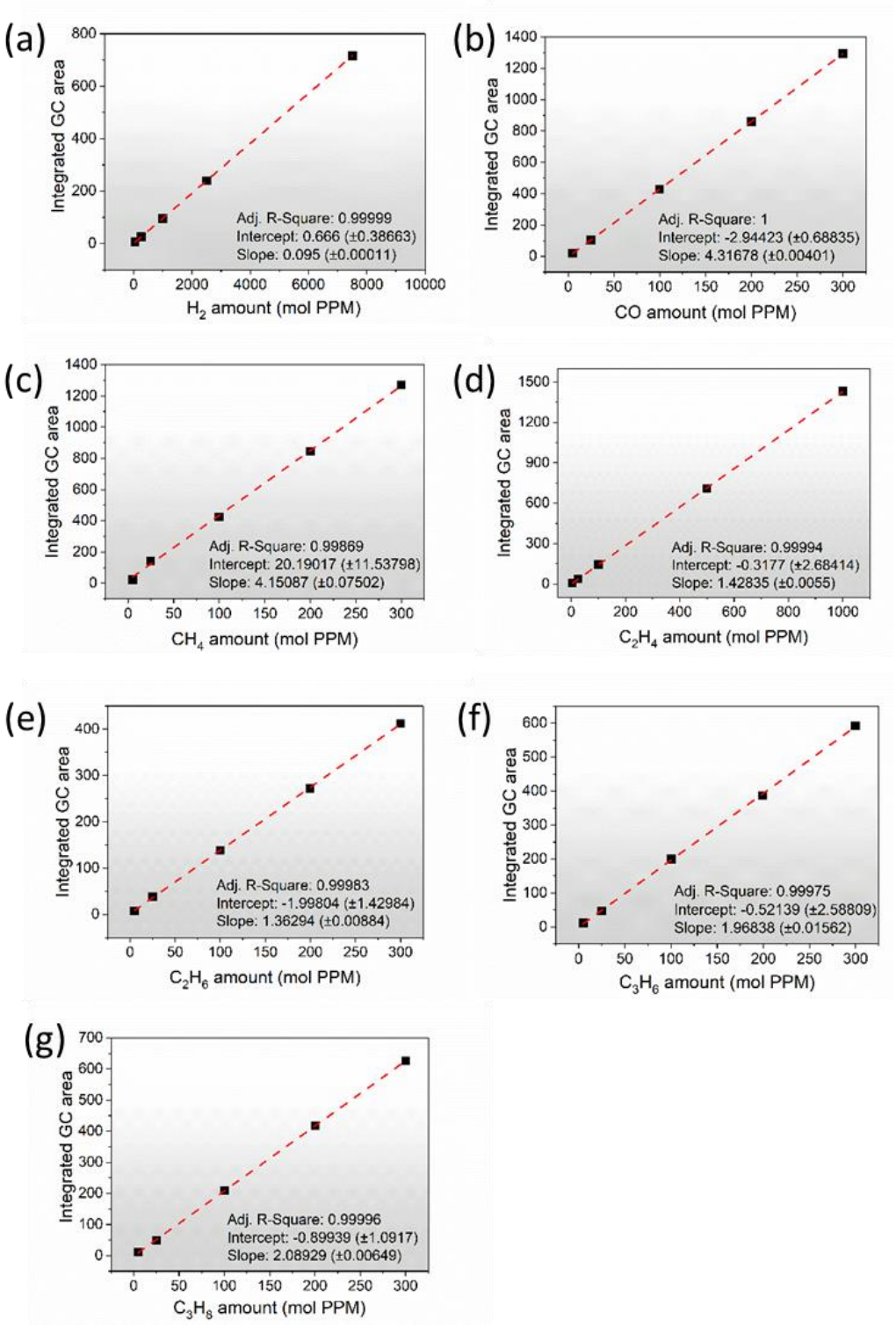

Figure S16: GC calibration plot for (a) H_2 (b) CO (c) CH_4 (d) C_2H_4 (e) C_2H_6 (f) C_3H_6 and (g) C_3H_8. Calibrations were performed at 20 sccm flowrate. The balance gas for all calibration gases is CO_2. Related to Figure 3.

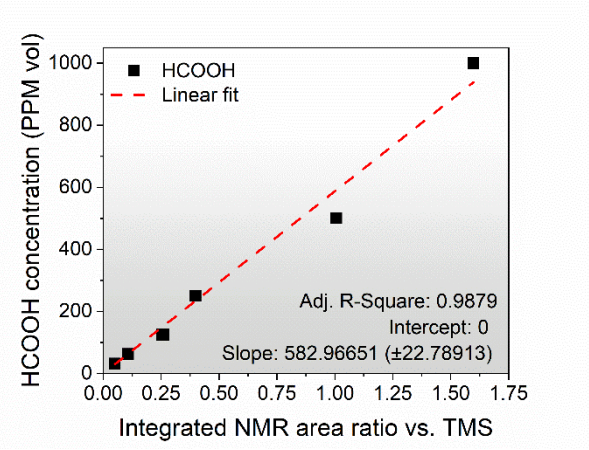

Figure S17: NMR calibration plot for formic acid. Mixtures of different concentrations of formic acid are prepared in the same composition of acetonitrile-H_2O-$BMIMBF_4$ mixture as the electrolyte used in this study. Integrated NMR area ratio is calculated with respect to the internal standard (50 mM tetramethyl silane in acetonitrile) area. Related to Figure 3.

Table S7: Surface energy of different types of Ti_2CT_x. The most favourable T_x surface termination sites (*fcc* or *hcp*) with lowest surface energy are marked in red. Related to Figure 4.

	Surface energy (eV)			
–F Substitution	0.0%	33.3%	66.7%	100.0%
fcc	-405.35	-390.44	-374.67	-357.66
hcp	-388.96	-377.74	-366.44	-352.73

Table S8: Surface energy of different types of Mo_2CT_x. The most favourable T_x surface termination sites (*fcc* or *hcp*) with lowest surface energy are marked in red. Related to Figure 4.

	Surface energy (eV)					
–F Substitution	0.0%	11.1%	22.2%	33.3%	66.7%	100.0%
fcc	-405.21	-402.96	-398.20	-394.17	-377.34	-358.09
hcp	-414.71	-409.59	-403.96	-397.10	-375.26	-355.50

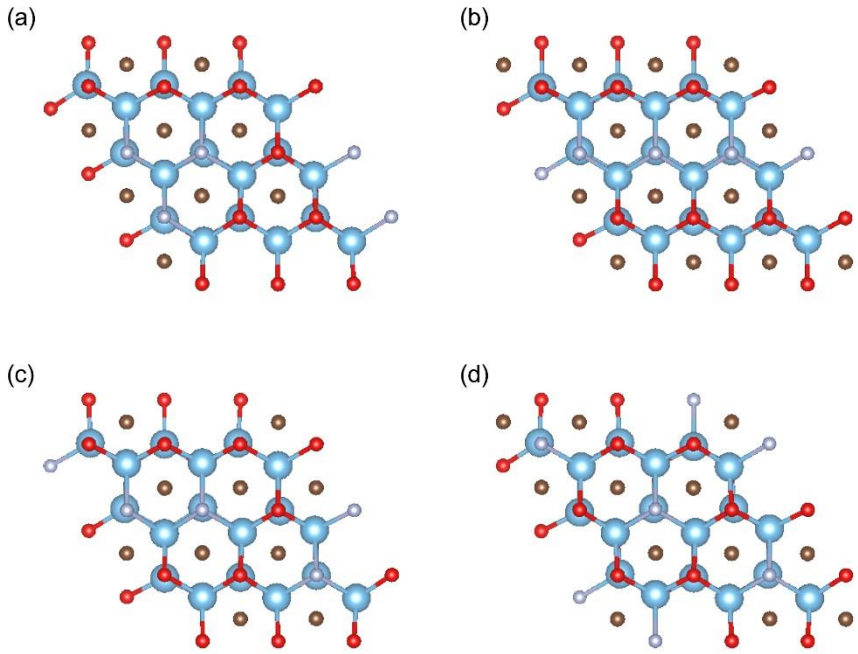

Figure S18: –F termination distribution pattern for 33.3% -F substituted Ti_2CT_x. The calculated energies are (a) -389.88 eV, (b) -389.95 eV, (c) -390.03 eV, and (d) -390.44 eV. Related to Figure 4.

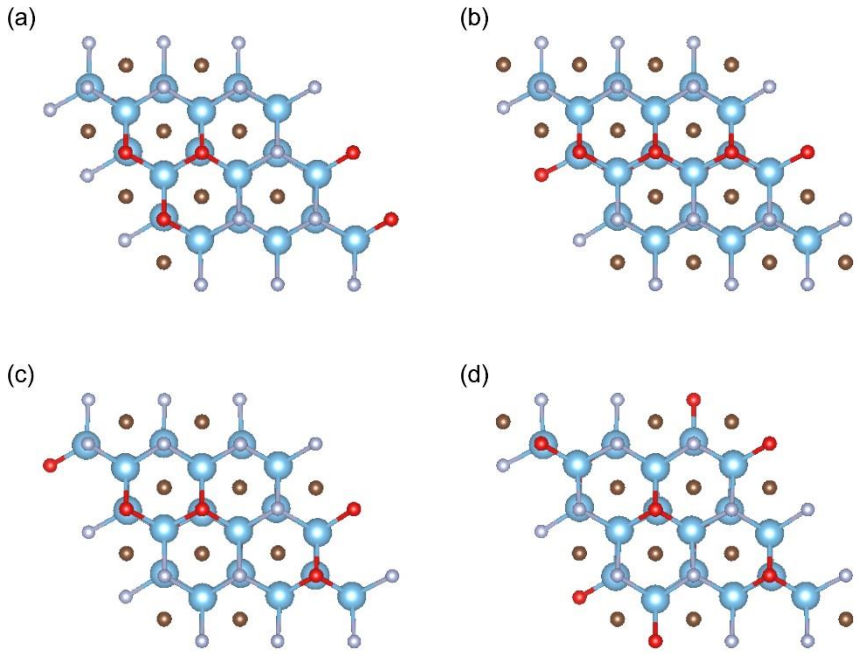

Figure S19: –F termination distribution pattern for 66.7% –F Ti_2CT_x. The calculated energies are (a) -374.11 eV, -374.21 eV, (c) -374.31 eV, (d) -374.67 eV. Related to Figure 4.

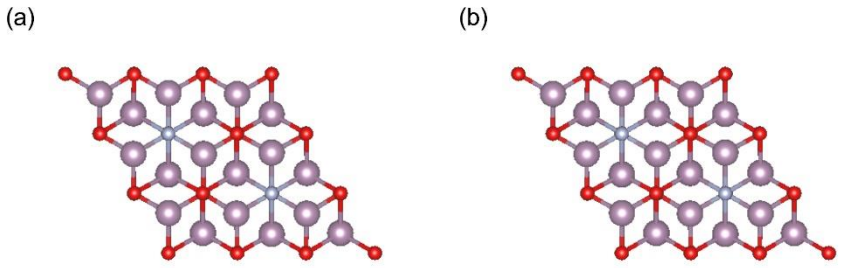

Figure S20: –F termination distribution pattern for 22.2% –F Mo_2CT_x. The calculated energies are (a) -403.66 eV, (b) -403.96 eV. Related to Figure 4.

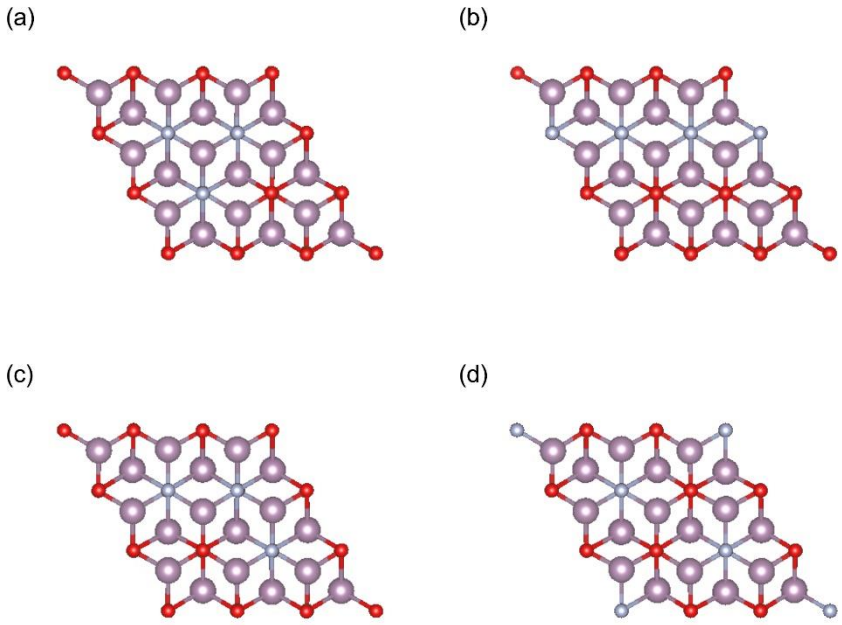

Figure S21: –F termination distribution pattern for 33.3% –F Mo_2CT_x. The calculated energies are (a) -396.26 eV (b) -396.32 eV (c) -396.46 eV (d) -397.10 eV. Related to Figure 4.

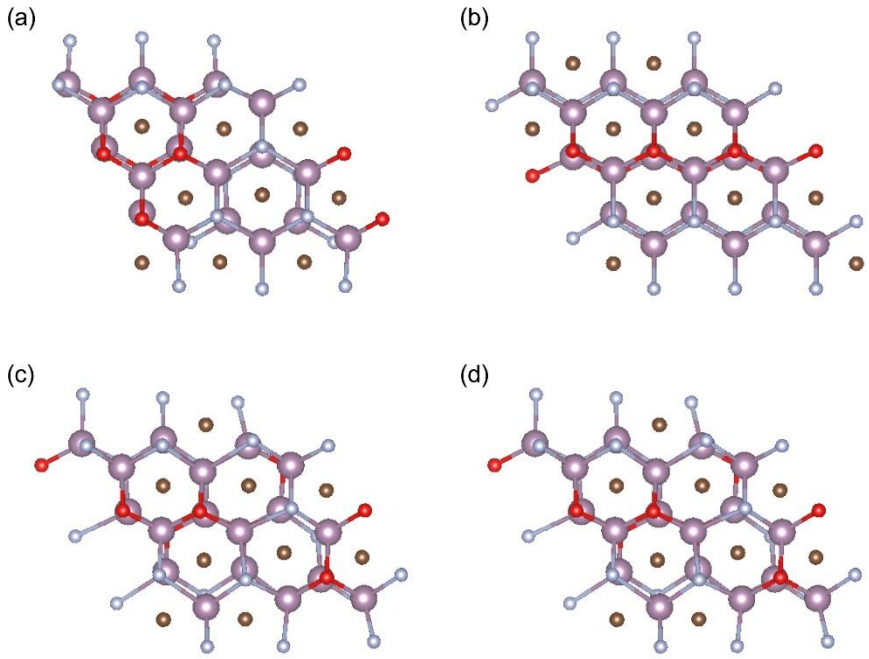

Figure S22: –F termination distribution pattern for 66.7% –F Mo_2CT_x. The calculated energies are (a) -377.15 eV, (b) -376.65 eV, (d) -376.26 eV, (d) -377.34 eV. Related to Figure 4.

Transparent Methods

Synthesis

Ti_2AlC was synthesised following previously reported procedure (Handoko et al., 2018). Typically, TiC, Ti, and Al powders (Alfa Aesar) with average particle sizes of 2 µm, <44 µm and <44 µm, respectively, were ball milled for 24 h using zirconia balls in a plastic jar. The TiC : Ti : Al molar ratio was 0.85 : 1.15 : 1.05. The powder mixture was heated in an alumina crucible at 5 ºC min^{-1} to 1400 ºC and held for 4 h under flowing Ar. After furnace cooling, the porous compact was milled using a TiN-coated milling bit and sieved through a 400 mesh sieve to make Ti_2AlC powder with particle size <37µm.

Mo_2Ga_2C synthesis methods were described previously (Hu et al., 2015). In brief, 2:1 molar ratio of Mo and C powders (Alfa Aesar) were first heated at 1000 °C for 12 h in Ar environment. The resulting Mo_2C solid was crushed into a powder and homogeneously mixed with melted Ga (at 45 °C) in mortar and pestle with 1:8 molar ratio. The solidified mixture was then vacuum sealed inside quartz tube. The quartz tube then heated at a rate of 10 °C min^{-1} to 850 °C, and held at that temperature for 48 h. The resulting powder was immersed in a 37 wt% HCl after cooling for 3 days to dissolve possible residual Ga or Ga_2O_3. The final Mo_2Ga_2C powders were sieved to achieve particle size of <37 µm and kept under argon filled glovebox until further use.

HF etched Ti_2CT_x and Mo_2CT_x MXenes were prepared as reported previously (Anasori et al., 2017). Typically, 2 g of Ti_2AlC or Mo_2Ga_2C powders were added slowly (over ≈2 min) onto 20 mL of 10 wt% (or 48 wt% for Mo_2Ga_2C) HF solution (Merck) and held for 18 h (or 7 days for Mo_2Ga_2C) at ambient temperature (or 55 ºC for Mo_2Ga_2C) inside a Teflon container while stirring at 200 rpm. After that the mixtures were washed at least 5 times by adding deionized (DI) water (18.2 MΩ•cm, Purelab Option Q), shaken for 1 min using a vortex shaker and centrifuging for 5 min at 5000 rpm until a pH of >6. The powders were then dried under vacuum at 50 °C and kept under argon filled glovebox until further use.

To make fluoride salt etched Ti_2CT_x (Liu et al., 2017), solution containing 4.70 g of KF (99%, Merck) is slowly mixed into 20 mL HCl (36-38%, electronic grade, Duksan Reagents) under magnetic stirring (200 rpm) for 10 minutes inside a Teflon container. Afterwards, 2 g of Ti_2AlC is poured slowly over 2 mins to the solution, and kept under stirring (200 rpm) for 48 h at 40 °C. The samples were then washed with DI water 5 times and ethanol 2 times until pH of supernatant is around 7. The powders were then dried under vacuum at 50 °C and kept under argon filled glovebox until further use.

Characterisation

Morphology of the materials are characterised using JEOL JSM-7600F Schottky Field Emission Scanning Electron Microscope (SEM) operating at 5 kV and 116 µA emission power. Gentle beam

mode is applied at a reduced 1 kV emission voltage to minimise surface charging on non-conductive precursor phases.

Phase composition of the materials was characterised using X-ray diffraction (XRD) using Bruker Advance D8 diffractometer (Cu Kα, λ = 1.541058 Å) fitted with Ni filter and LynxEye XE energy dispersive 1-D detector at 40 kV 40 mA operating power. Coupled θ-2θ scans were performed from 3 to 85° 2θ range with 0.02° step size and 0.3 s time per step. A motorised variable aperture was programmed to provide a fixed 10 mm sample irradiation length to enhance signals at higher 2θ angles. A beam knife is fitted about 1 mm above the sample to minimise air scattering signal at low 2θ angles. Powders were packed into a zero background diffraction plate with ⌀10 mm × 0.2 mm cavity depth (off-cut Si, MTI Corporation) to reduce background contribution.

Elemental analyses is done using X-ray photoelectron spectroscopy (XPS) using a Thermo ThetaProbe or Kratos Axis Supra with a monochromatic Al Kα X-ray source (1486.7 eV). Two consecutive measurements were conducted. The first is to obtain energy calibration signal from adventitious C *1s* peak at 284.8 eV. The second measurement was performed after sputtering the sample with Ar^+ ion gun for ~600 s to remove surface contamination and better identify C *1s*, Ti *2p* or Mo *3d* components belonging to MXene. XPS fitting was done using Avantage software (V6.01, Thermo Scientific), with fitting assignment following the literature (Mashtalir et al., 2013, Halim et al., 2016).

Electrochemical CO_2 reduction

All CO_2RR were performed inside a custom made, two-compartment PTFE electrochemical cell at room temperature (23-25 °C). Each compartment is of 11 mL volume, and separated by 7×2 cm^2 Nafion 117 membrane (Chemours). The cathodic compartment is filled with 8 mL mixture of acetonitrile (80 mol%, HPLC grade, VWR Chemicals) and DI water (15 mol%, 18.2 MΩ•cm, Purelab Option-Q) as solvent, with 3-butyl-1-methyl-1H-imidazol-3-ium tetra-fluoroborate ionic liquid (5 mol%, $BMIMBF_4$, 98%, Combi Blocks) added in as supporting electrolyte. The pH of the electrolyte is 1.24. The addition of water is essential as a proton source and to manage the solution viscosity.(Rosen et al., 2013, Yang et al., 2019) The anodic compartment is filled with 8 mL of 0.5 M H_2SO_4 (Merck Ultrapur) as proton reservoir (Lu et al., 2018).

A leakless Ag/AgCl (eDAQ) was used as reference electrode, placed 2 mm above the working electrode. The reference was calibrated with ferrocene and the potential in this work is reported against SHE, by taking the average redox potential of Fc/Fc^+ to be 0.624 V vs. SHE in acetonitrile solution at 25 °C (Pavlishchuk and Addison, 2000). Electrochemical measurements were done using a calibrated potentiostat (Gamry 600+ or Gamry 3000). Electrolyte resistance was measured each time using high frequency electrochemical impedance spectroscopy and compensated using positive feedback correction at 85% level. The typical R_u compensation applied is around 8.5-9.5 Ω.

The working electrode substrate is ⌀15 mm x 1 mm vitreous carbon discs (Goodfellow), polished to mirror finish with 1 μm alumina slurry followed by 0.3 μm alumina slurry (Buehler). After each polishing steps, the substrate is ultrasonicated in DI water twice for 5 minutes each. To prepare the catalyst ink, 5 mg of MXene is added into 0.6 mL DI water and 0.4 mL ethanol (absolute grade, VWR Chemicals) and 40 uL of Nafion solution (5% mixture in lower aliphatic alcohol and water, Sigma Aldrich). The ink is then homogenised in an ice bath (*approx.* 0-4 °C) inside an ultrasonicator for 15 minutes, vortex shaken (2400 rpm) for 1 minute and deposited volumetrically onto the polished glassy carbon to achieve 0.5 mg cm^{-2} loading per vitreous carbon substrate. The catalyst ink is then dried under table lamp (100 W lightbulb). The exposed geometric surface area is 1.327 cm^2. Spectroscopically pure graphite rod (Ted Pella) was used as the counter electrode.

CO_2 gas (99.999%, Linde Gas) was delivered to both compartments of the electrochemical cell using calibrated mass flow controller (MC 100SCCM-D, Alicat Scientific) at 20 sccm flowrate. The samples were subjected to chronoamperometric (constant voltage) measurement for 100 mins under continuous CO_2 gas purging. Periodic sampling every 12.45 minutes was done by an online custom valve gas chromatograph (GC; Wasson-ECE) for gas products quantification. The GC is equipped with a thermal conductivity detector (N_2 carrier gas, 99.9995%, Leeden National Oxygen) for detecting H_2 and flame ionization detectors (He carrier gas, 99.9995%, Leeden National Oxygen) with a methaniser for detecting C_1 to C_3 hydrocarbons and CO. Chromatograms were processed using Openlab CDS (Chemstation edition, rev. C.01.08, Agilent Technologies). Gaseous products were calibrated with 6 standard gas mixtures in CO_2 balance gas. (AG Gases Ltd., mixtures traceable to standards at the National Physical Laboratory, UK).

Liquid products were analysed using 500 MHz nuclear magnetic resonance (NMR; JEOL JNM-ECA500II), operated with DANTE selective excitation sequence (Morris and Freeman, 1978) (2 μs pulse, 0.1 ms interval, 40 dB RF output) to suppress high concentration solvent signals. Each spectra is an average of 64-128 consecutive scans. Data was processed using JEOL Delta V5.2. To prepare sample for NMR analysis, 1 mL of sample is mixed with 50 uL of internal standard (50 mM tetramethyl silane in acetonitrile, Cambridge Isotope Lab, 99.9%). 0.5 mL of this mixture is then mixed with 0.1 mL of acetonitrile-D_3 (Cambridge Isotope Lab, 99% D). NMR calibration is performed using variable concentrations of formic acid in acetonitrile-H_2O-$BMIMBF_4$ electrolyte in the presence of internal standard and acetonitrile-D_3. The Faradaic efficiency was calculated by comparing the number of electrons required for the amounts of detected products and the recorded number of electrons measured by the potentiostat (Ren et al., 2015).

DFT calculation details

First-principle calculation in the framework of density functional theory (DFT) was applied for all the simulations by using the Vienna ab-initio Simulation Package (VASP) (Kresse and Furthmüller, 1996).

The projector-augmented-wave (PAW) pseudopotential was adopted to treat the core electrons (Blöchl, 1994). Perdew-Burker-Ernzehof (PBE) formulation based on the generalized gradient approximation (GGA) exchange-correlation was utilized to simulate the electron interactions (Perdew et al., 1996). To take Van der Waals force into consideration, correction using DFT-D3 formalism is adopted (Grimme et al., 2010, Grimme et al., 2011). A cut-off energy 450 eV was applied for all computations. Geometry optimization process were fully carried out, and the energy convergence criteria on each atom was 0.03 eV $Å^{-1}$. The thickness of vacuum is at least 20 Å to avoid artificial interactions amongst the periodic slabs. The 3×3×1 Monkhorst-Pack *k*-point mesh sampled Brillouin zone was used for 3×3 supercells.

The computational hydrogen electrode (CHE) was employed, avoiding the explicit treatment of solvated protons (Nørskov et al., 2005). The change of free energy at 0 V (*vs.* RHE) can be calculated by the following equation:

$$\Delta G = \Delta E_{elec} + \Delta E_{ZPE} - T \times \Delta S$$

Where ΔE_{elec} is the electronic energy difference between two contiguous reaction steps, ΔE_{ZPE} is the difference of the zero-point energy, T is the temperature and assumed as 298.15 K, while ΔS is the difference of the entropy. *ZPE* and vibrational entropy of adsorbates are calculated from vibrations by standard methods, which is treated in the harmonic oscillator approximation (Cramer and Bickelhaupt, 2003). As for the gas-phase molecule, the thermal corrections of translations and rotations is also included.

Prior to calculating CO_2RR intermediates, the most preferred T_x sites with lowest energy for four Ti_2CT_x and five Mo_2CT_x models with varying –F substitution levels are first determined. The different distributions of –F atoms at various substitution levels to –O T_x groups are also taken into consideration. Mo_2CT_x models with 66.7% and 100% –F substitution are excluded from further calculations due to significant structure distortion. Ti_2CT_x with 100% –F substitution is also excluded due to unstable intermediate adsorption.

Supplemental references

Anasori, B., Lukatskaya, M. R. & Gogotsi, Y. 2017. 2D metal carbides and nitrides (MXenes) for energy storage. *Nat. Rev. Mater.,* 2**,** 16098.

Blöchl, P. E. 1994. Projector augmented-wave method. *Phys. Rev. B,* 50**,** 17953.

Cramer, C. J. & Bickelhaupt, F. 2003. Essentials of Computational Chemistry. *Angew. Chem. Int. Edit.,* 42**,** 381-381.

Grimme, S., Antony, J., Ehrlich, S. & Krieg, H. 2010. A consistent and accurate ab initio parametrization of density functional dispersion correction (DFT-D) for the 94 elements H-Pu. *J. Chem. Phys.,* 132**,** 154104.

Grimme, S., Ehrlich, S. & Goerigk, L. 2011. Effect of the damping function in dispersion corrected density functional theory. *J. Comput. Chem.,* 32**,** 1456-1465.

Halim, J., Kota, S., Lukatskaya, M. R., Naguib, M., Zhao, M.-Q., Moon, E. J., Pitock, J., Nanda, J., May, S. J., Gogotsi, Y. & Barsoum, M. W. 2016. Synthesis and Characterization of 2D Molybdenum Carbide (MXene). *Adv. Funct. Mater.,* 26**,** 3118-3127.

Handoko, A. D., Fredrickson, K. D., Anasori, B., Convey, K. W., Johnson, L. R., Gogotsi, Y., Vojvodic, A. & Seh, Z. W. 2018. Tuning the Basal Plane Functionalization of Two-Dimensional Metal Carbides (MXenes) To Control Hydrogen Evolution Activity. *ACS Appl. Energy Mater.,* 1**,** 173-180.

Hu, C., Lai, C. C., Tao, Q., Lu, J., Halim, J., Sun, L., Zhang, J., Yang, J., Anasori, B., Wang, J., Sakka, Y., Hultman, L., Eklund, P., Rosen, J. & Barsoum, M. W. 2015. Mo_2Ga_2C: a new ternary nanolaminated carbide. *Chem. Commun.,* 51**,** 6560-6563.

Kresse, G. & Furthmüller, J. 1996. Efficient iterative schemes for ab initio total-energy calculations using a plane-wave basis set. *Phys. Rev. B,* 54**,** 11169.

Liu, F., Zhou, A., Chen, J., Jia, J., Zhou, W., Wang, L. & Hu, Q. 2017. Preparation of Ti_3C_2 and Ti_2C MXenes by fluoride salts etching and methane adsorptive properties. *Appl. Surf. Sci.,* 416**,** 781-789.

Lu, L., Sun, X., Ma, J., Yang, D., Wu, H., Zhang, B., Zhang, J. & Han, B. 2018. Highly Efficient Electroreduction of CO_2 to Methanol on Palladium–Copper Bimetallic Aerogels. *Angew. Chem. Int. Ed.,* 57**,** 14149-14153.

Mashtalir, O., Naguib, M., Mochalin, V. N., Dall'Agnese, Y., Heon, M., Barsoum, M. W. & Gogotsi, Y. 2013. Intercalation and delamination of layered carbides and carbonitrides. *Nat. Commun.,* 4**,** 1716.

Morris, G. A. & Freeman, R. 1978. Selective excitation in Fourier transform nuclear magnetic resonance. *J. Magn. Reson.,* 29**,** 433-462.

Nørskov, J. K., Bligaard, T., Logadottir, A., Kitchin, J., Chen, J. G., Pandelov, S. & Stimming, U. 2005. Trends in the exchange current for hydrogen evolution. *J. Electrochem. Soc.,* 152**,** J23-J26.

Pavlishchuk, V. V. & Addison, A. W. 2000. Conversion constants for redox potentials measured versus different reference electrodes in acetonitrile solutions at 25°C. *Inorg. Chim. Acta,* 298**,** 97-102.

Perdew, J. P., Burke, K. & Ernzerhof, M. 1996. Generalized gradient approximation made simple. *Phys. Rev. Lett.,* 77**,** 3865.

Ren, D., Deng, Y., Handoko, A. D., Chen, C. S., Malkhandi, S. & Yeo, B. S. 2015. Selective Electrochemical Reduction of Carbon Dioxide to Ethylene and Ethanol on Copper(I) Oxide Catalysts. *ACS Catal.,* 5**,** 2814-2821.

Rosen, B. A., Zhu, W., Kaul, G., Salehi-Khojin, A. & Masel, R. I. 2013. Water Enhancement of CO_2 Conversion on Silver in 1-Ethyl-3-Methylimidazolium Tetrafluoroborate. *J. Electrochem. Soc.,* 160**,** H138-H141.

Yang, D., Zhu, Q., Chen, C., Liu, H., Liu, Z., Zhao, Z., Zhang, X., Liu, S. & Han, B. 2019. Selective electroreduction of carbon dioxide to methanol on copper selenide nanocatalysts. *Nat. Commun.,* 10**,** 677.